RSC Advances

PAPER

View Article Online
View Journal | View Issue

Cite this: *RSC Adv.*, 2026, **16**, 26099

Design, synthesis, antimicrobial and antioxidant evaluation, cytotoxicity assessment, and molecular dynamics-based computational studies of novel PABA analogues as dual DHPS/DHFR inhibitors

Bhargav Devliya,[a] Ahmed K. Al-Kubeisi,[b] Drashti Patel,[c] Milan Dabhi,[c] Bimalkumar Patel,[a] Milan Thakar,[d] Jaykumar Nagapara,[a] Shreya Chauhan,[g] Kiransinh Rajput,[c] Dweipayan Goswami,[c] Nandan Dixit,[e] Saumya K. Patel,[e] Gaurang Sindhav,[d] Botros Y. Beshay[f] and Hitesh D. Patel *[a]

The rapid emergence of antimicrobial resistance (AMR) has become a global threat, limiting the clinical effectiveness of the drugs against microbial infections. As Methicillin-resistant *Staphylococcus aureus* (MRSA) and Extensively drug-resistant (XDR) *Escherichia coli* continue to evolve rapidly, it is critical to develop novel therapeutic agents and structurally unique antibacterial medicines. The selective bacterial folate biosynthesis pathway, which includes dihydropteroate synthase (DHPS) and dihydrofolate reductase (DHFR), represents an attractive therapeutic target; however, the alarming rise of microbial sulfonamides necessitates the development of novel inhibitors. Sulphonamide antibiotics are analogues of *p*-aminobenzoic acid (PABA), which serves as a substrate for folate biosynthesis. Taking this into account, we developed novel PABA-imidazole analogues to combat antimicrobial resistance. In this study we designed and synthesized seven novel PABA analogues and characterized them by various spectroscopy techniques. These synthesized PABA analogues show comparatively better efficiency against both the Gram-positive (*S. aureus* and *S. pyogenes*) and Gram-negative (*E. coli* and *P. aeruginosa*) strains. Furthermore, they also show potential activity against MRSA and XDR *E. coli*. The DHPS/DHFR enzyme assay demonstrated that the **SB2** compound suppresses the sulfamethoxazole (SUL) in DHPS inhibition, and the **SB5** compound shows comparatively increased DHFR inhibitory activity compared to the trimethoprim (TMP). These results have been validated by molecular dynamics simulations and free energy analyses. In addition, the lead compounds also showed strong antioxidant activity, low cytotoxicity, and good DNA nicking behaviour, which supports their therapeutic potential.

Received 6th March 2026
Accepted 11th May 2026

DOI: 10.1039/d6ra01925k

rsc.li/rsc-advances

1. Introduction

AMR, a global health crisis, accounted for approximately 4.95 million fatalities in 2019. If current trends persist, the mortality burden is projected to reach nearly 10 million deaths annually by 2050, potentially surpassing cancer as a leading cause of death.[1] This challenge spans multiple sectors, including medicine, agriculture, and the economy, underscoring its significance as an important global health concern. The 2030 United Nations Sustainable Development Goals also include specific targets addressing AMR. Furthermore, median resistance levels of 42% for third-generation cephalosporin-resistant *E. coli* and 35% for MRSA across 76 countries further accentuate the urgency of intervention.[2–4] Due to antibiotic misuse and overuse, the increasing emergence of resistant bacterial strains necessitates the development of novel therapeutic strategies and antimicrobial agents with distinct mechanisms of action. Current antibacterial modes of action include cell wall synthesis, nucleic acid replication, bacteriophage therapy, antimicrobial combination therapy, nanotechnology, and metabolic or enzymatic pathway inhibition.[5] One strategy for tackling bacterial antibiotic resistance is to target compromised

[a]*Department of Chemistry, School of Sciences, Gujarat University, Ahmedabad, India. E-mail: drhiteshpatel1@gmail.com*

[b]*College of Pharmacy, University of Almaarif, Al Anbar, 31001, Iraq*

[c]*Department of Microbiology, School of Sciences, Gujarat University, Ahmedabad, India*

[d]*Department of Zoology, School of Sciences, Gujarat University, Ahmedabad, India*

[e]*Department of Bioinformatics, School of Sciences, Gujarat University, Ahmedabad, India*

[f]*Pharmaceutical Sciences (Pharmaceutical Chemistry) Department, College of Pharmacy,Arab Academy for Science, Technology and Maritime Transport, P.O. Box 1029, Alexandria, Egypt*

[g]*Department of Environmental Science, School of Sciences, Gujarat University, Ahmedabad, India*

or mutated biological structure-based drug designs to overcome resistance mechanisms.[5]

Metabolic targets in the folate biosynthesis pathway represent attractive and selective targets because prokaryotes and lower eukaryotes depend on this pathway for *de novo* folate synthesis, whereas higher eukaryotes obtain folate through dietary intake.[6] Due to the absence of DHPS in higher organisms and its widespread presence in microorganisms, sulfonamides, among the first successful antimicrobial drugs, served as effective broad-spectrum agents by inhibiting DHPS and disrupting folate metabolism. However, their effectiveness has been progressively compromised by the rapid rise of bacterial resistance.[7,8] Sulfonamide resistance emerged through multiple mechanisms, including mutations in the DHPS enzyme, acquisition of alternative DHPS genes, overproduction of PABA to competitively inhibit drug binding, and efflux pump activity.[7,9,10] Additionally, sulfonamides are accompanied by significant adverse effects.[11] Although antimicrobial resistance continues to rise, the folate biosynthesis pathway has not been fully explored, particularly with respect to the simultaneous inhibition of both DHPS and DHFR, as classical sulfonamides primarily target DHPS alone. This research gap underscores the necessity of structurally novel PABA analogues that can evade resistance, enhance potency, and reduce toxicity. To address this, we employed *in silico* approaches to explore drug–protein interactions of functionalized sulfonamide derivatives and to rationally modify existing scaffolds for the development of effective dual inhibitors.

In the present study, we designed a novel series of PABA analogues containing an imidazole-thio pharmacophore to target the bacterial folate biosynthesis pathway. Seven compounds were synthesized through conventional heating and microwave-assisted methods and characterized by standard spectroscopy techniques. The antimicrobial potential was evaluated against two Gram-positive (*S. aureus* and *S. pyogenes*) and two Gram-negative strains (*E. coli* and *P. aeruginosa*) and further evaluated against MRSA and XDR *E. coli*. The mechanism of action was evaluated by DHPS/DHFR enzyme inhibition assays, oxidative stress analysis, DNA interaction studies, and cytotoxicity evaluation. Also, molecular dynamics simulations and binding free energy calculations were performed for the most promising lead compounds identified experimentally. Overall, this study demonstrates the potential of PABA-imidazole hybridization as a viable strategy for the development of dual DHPS/DHFR inhibitors. This dual-targeting strategy is expected to reduce resistance development by simultaneously inhibiting sequential enzymes in the folate pathway.

2. Rational molecular design approach

To improve the antifolate activity, this study focuses on modification of the PABA scaffold through a rational molecular design strategy. The approach involves combining key pharmacophoric scaffolds within a single framework while using PABA itself as a natural substrate for the bacterial enzyme DHPS. The approach preserves the aromatic amino-benzoate structure, allowing for structural flexibility while retaining target affinity. Through molecular hybridization approach, PABA is attached to a bioactive heterocyclic fragment to develop a dual-functional hybrid molecule capable of overcoming the limitations of conventional sulfonamides. The basic structure of the PABA-based scaffold has been modified in the designed analogues to improve interaction and binding affinity with the target enzyme while retaining the essential PABA core. The modification was selectively introduced at the amino group of PABA, as functionalization at this position retains the biological relevance of the aromatic carboxylic acid moiety.[12,13] A linker chloroacetyl chloride, is attached to facilitate conjugation with another bioactive molecule.

The imidazole-mercapto-substituted heterocyclic moiety 1-(2-mercapto-1-(4-methoxyphenyl)-4-methyl-1*H*-imidazole-5-yl) ethan-1-one was selected as the second scaffold based on its relevance in previously reported studies and established activity

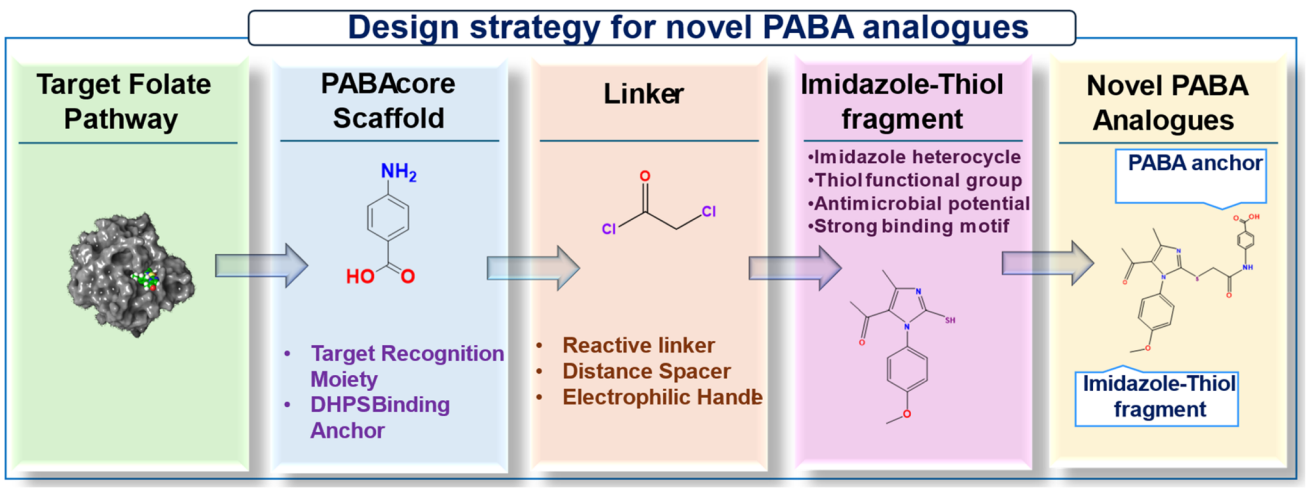

Fig. 1 Rational design approach for the synthesis of novel PABA analogues.

of imidazole-containing scaffolds.[14,15] Imidazole and imidazole-thio-containing moieties are recognized as potent antimicrobial and antifungal pharmacophores.[14,15] The novelty of the present design lies in the hybridization of an active imidazole-thio moiety with the PABA scaffold *via* an acetyl linker (Fig. 1). This approach is expected to enable synergistic activity, where the PABA scaffold targets the folate metabolic pathway and the heterocyclic moiety contributes additional antimicrobial efficacy. This design is expected to reduce resistance development by simultaneously leveraging substrate mimicry (PABA) and the intrinsic antimicrobial activity of the heterocyclic moiety, thereby enabling a dual-targeting strategy within the folate biosynthesis pathway.

3. Material and methods

3.1 Chemistry

3.1.1 Chemicals and reagents. *p*-Methoxy aniline, 3-chloro-2,4-pentanedione, potassium thiocyanate, ammonium thiocyanate, triethylamine, chloroacetyl chloride, and the required PABA analogues were purchased from standard chemical suppliers and used without further purification. Ethanol, dichloromethane (DCM), and dimethylformamide (DMF) were used as solvents. Anhydrous sodium sulfate, potassium carbonate, sodium bicarbonate, brine, and ice were used for workup and purification steps. All reactions were carried out under standard laboratory conditions with monitoring by thin-layer chromatography (TLC). The synthesized compounds were characterized by using Fourier transform infrared (FTIR) spectroscopy, ^{1}H, ^{13}C, and ^{19}F nuclear magnetic resonance (NMR) spectroscopy, and mass spectroscopy. FTIR analysis was performed to identify the functional groups, while NMR spectra were used to confirm the structural integrity and proton and carbon environment. Mass spectra were performed to confirm the molecular mass of the compounds. Since no nitrosating agents or conditions such as nitrites in an acidic environment were used during the reaction, the possibility of nitrosamines being formed is negligible.

3.1.2 Synthesis of compound S, 1-(2-mercapto-1-(4-methoxyphenyl)-4-methyl-1*H*-imidazole-5-yl)ethan-1-one. The 1-(2-mercapto-1-(4-methoxyphenyl)-4-methyl-1*H*-imidazole-5-yl) ethan-1-one was prepared according to the literature procedure (Scheme 1).[14,15]

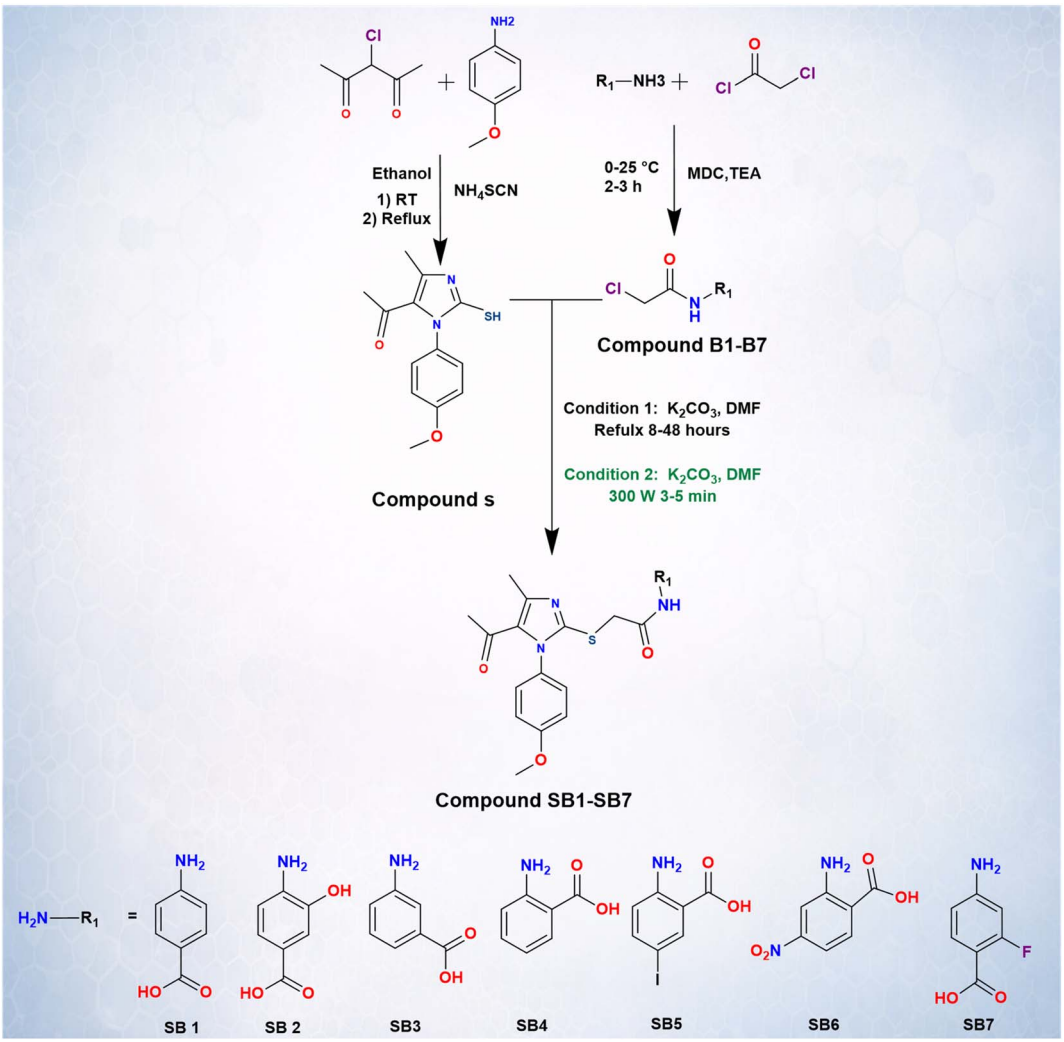

Scheme 1 Reaction procedure for the synthesis of compounds SB-SB7.

Light brown solid; 95% yield; MS (ESI) *m/z*: 263 $[M + H]^+$; ^{1}H NMR (400 MHz, DMSO-d_6) δ: 10.55 (s, 1H, S–H), 7.49 (d, J = 8.4 Hz, 2H), 6.93 (d, J = 8.4 Hz, 2H), 3.73 (s, 3H, OCH_3), 2.507 (s, 3H, $COCH_3$), 2.37 (s, 3H, CH_3); ^{13}C NMR (100 MHz, DMSO-d_6): δ 188.14, 166.53, 157.39, 155.58, 133.71, 122.05, 120.36, 114.78, 55.64, 50.57, 30.01, 18.89.

3.1.3 Synthesis of (2-chloroacetamido)benzoic acid derivatives (B1–B7). A solution of the desired PABA analogue (0.01 mol) in dry dichloromethane (DCM) (20 mL) was cooled to 0–5 °C, and triethylamine (TEA) (0.012 mol) was added to the stirred mixture. To this chilled solution, chloroacetyl chloride (0.012 mol) was added dropwise over 10 minutes while maintaining the temperature below 5 °C. After the addition, the reaction mixture was stirred for 1 hour at 0–5 °C and then for 1 hour at room temperature. The reaction was quenched with ice-cold saturated sodium bicarbonate solution, and the layers were separated. The organic layer was washed with brine solution, dried over anhydrous sodium sulfate, filtered, and evaporated under vacuum. The crude product was recrystallized using ethanol to obtain compounds **B1–B7** (Scheme 1).

3.1.4 Synthesis of (2-((5-Acetyl-1-(4-methoxyphenyl)-4-methyl-1*H*-imidazole-2-yl)thio)acetamido) benzoic acid derivatives (SB1–SB7). A mixture of compound **S** (1 mmol) and the appropriate (2-chloroacetamido) benzoic acid derivative (**B1–B7**, 1 mmol) in DMF (10 mL) was treated with potassium carbonate (K_2CO_3) (2 mmol) under stirring. The reaction mixture was refluxed for 6 hours, and the progress was monitored by TLC (Scheme 1). Upon completion, the reaction mixture was cooled to room temperature and poured into cold water to precipitate the solid. The resulting solid was filtered, washed with water, and recrystallized using ethanol to obtain the desired compounds **SB1–SB7** in good yield.

3.1.5 Microwave-assisted green synthesis of compounds SB1–SB7. For microwave-assisted synthesis, the same reactants and solvent were used, with K_2CO_3 (1 mmol) as a base. The mixture was exposed to microwave irradiation at 450 W for 2–5 minutes, followed by refluxing until completion, monitored by TLC. The reaction mixture was cooled, diluted with water, and the solid product was collected by filtration and recrystallized from ethanol.

*3.1.5.1 4-(2-((5-Acetyl-1-(4-methoxyphenyl)-4-methyl-1H-imidazole-2-yl)thio)acetamido)benzoic acid (**SB1**).* Pale yellow solid; yield 90%; IR (ν_{max}, cm^{-1}): 3270 (N–H), 2921, 2850 (C–H), 1685 (C=O), 1585–1503 (Ar C=C), 1247–1020 (C–O/C–N); MS (ESI) *m/z*: 440 $[M + H]^+$; ^{1}H NMR (400 MHz, DMSO-d_6) δ: 10.665 (s, 1H, NH), 7.81 (d, J = 8.4 Hz, 2H, Ar–H), 7.52–7.49 (m, 4H, Ar–H), 7.07 (d, J = 8.4 Hz, 2H, Ar–H), 4.73 (s, 2H, S–CH_2), 3.78 (s, 3H, OCH_3), 2.508 (s, 3H, $COCH_3$), 2.45 (s, 3H, CH_3). The exchangeable carboxylic acid (COOH) proton was not observed, likely due to rapid solvent-mediated exchange; ^{13}C NMR (100 MHz, DMSO-d_6): δ 189.227, 175.033, 171.648, 169.773, 166.704, 159.328, 157.867, 139.699, 137.590, 136.379, 130.837, 130.082, 128.929, 123.285, 119.050, 118.050, 115.662, 112.655, 62.145, 55.907, 55.545, 40.588, 30.031, 28.343, 18.996.

*3.1.5.2 4-(2-((5-Acetyl-1-(4-methoxyphenyl)-4-methyl-1H-imidazole-2-yl)thio)acetamido)-3-hydroxybenzoic acid (**SB2**).* Yellow solid; yield 88%; IR (ν_{max}, cm^{-1}): 3412 (phenolic O–H), 3278 (N–H), 2931, 2860 (C–H), 1669–1685 (C=O), 1604–1585 (Ar C=C), 1495–1339, 1247–1020 (C–O/C–N), 937–721 (Ar C–H). MS (ESI) *m/z*: 456 $[M + H]^+$, 454 $[M + H]^-$; ^{1}H NMR (400 MHz, DMSO-d_6) δ: 13.66 (s, 1H, COOH), 11.36 (s, 1H, phenolic OH), 10.45 (s, 1H, NH), 7.73 (d, J = 8.8 Hz, 1H), 7.52 (m, 2H, Ar–H), 7.33 (d, J = 2.0 Hz, 1H, Ar–H), 7.13–7.06 (m, 3H, Ar–H), 4.718 (s, 2H, S–CH_2), 3.79 (s, 3H, OCH_3), 2.50 (s, 3H, $COCH_3$), 2.46 (s, 3H, CH_3); ^{13}C NMR (100 MHz, DMSO-d_6): δ 189.274, 172.002, 171.518, 171.460, 167.682, 167.279, 163.785, 162.568, 160.138, 159.405, 157.772, 157.721, 145.488, 144.745, 137.529, 131.640, 128.945, 123.484, 122.453, 115.699, 115.187, 111.210, 110.607, 108.274, 107.525, 106.366, 55.889, 55.752, 55.624, 40.585, 30.022, 18.966.

*3.1.5.3 3-(2-((5-Acetyl-1-(4-methoxyphenyl)-4-methyl-1H-imidazole-2-yl)thio)acetamido)benzoic acid (**SB3**).* Yellow solid; yield 85%; IR (ν_{max}, cm^{-1}): 3254 (N–H), 2924, 2853 (C–H), 1684 (C=O), 1605 (Ar C=C), 1237, 1168, 1107–1027 (C–O/C–N), 910, 842, 790, 735 (Ar C–H). MS (ESI) *m/z*: 440 $[M + H]^+$; ^{1}H NMR (400 MHz, DMSO-d_6) δ: 12.19 (s, 1H, COOH), 8.57 (d, J = 8.4 Hz, 1H, Ar–H), 8.01 (d, J = 8.0 Hz, 1H, Ar–H), 7.603–7.561 (m, 3H, Ar–H), 7.164–7.061 (m, 3H, Ar–H), 4.72 (s, 2H, S–CH_2), 3.97 (s, 3H, OCH_3), 2.50 (s, 3H, $COCH_3$), 2.46 (s, 3H, CH_3); ^{13}C NMR (100 MHz, DMSO-d_6): δ 189.491, 171.896, 170.247, 167.373, 159.428, 157.522, 140.897, 137.489, 134.185, 131.721, 128.679, 124.268, 123.273, 119.894, 115.809, 67.258, 57.223, 55.893, 40.596, 31.756, 30.842, 30.000, 29.456, 22.563, 18.975, 14.416.

*3.1.5.4 2-(2-((5-Acetyl-1-(4-methoxyphenyl)-4-methyl-1H-imidazole-2-yl)thio)acetamido)benzoic acid (**SB4**).* Yellow solid; yield 83%. IR (ν_{max}, cm^{-1}): 3325, 3273 (N–H/O–H stretching), 3080, 2921, 2851 (aromatic and aliphatic C–H stretching), 1685–1642 (amide I, C=O stretching), 1553 (amide II, N–H bending/C–N stretching), 1611–1509 (aromatic C=C stretching), 1354–1058 (C–O/C–N stretching), 1018–663 (aromatic C–H out-of-plane bending). MS (ESI) *m/z*: 440 $[M + H]^+$; ^{1}H NMR (400 MHz, DMSO-d_6) δ: 12.99 (s, 1H, COOH), 10.38 (s, 1H, NH), 8.267 (s, 1H, Ar–H), 7.77 (d, J = 7.6 Hz, 1H, Ar–H), 7.64 (d, J = 8.0 Hz, 1H, Ar–H), 7.53 (d, J = 8.8 Hz, 2H, Ar–H), 7.455–7.416 (m, 1H, Ar–H), 7.07 (d, J = 8.8 Hz, 2H, Ar–H), 4.713 (s, 2H, S–CH_2), 3.79 (s, 3H, OCH_3), 2.55 (s, 3H, $COCH_3$), 2.46 (s, 3H, CH_3); ^{13}C NMR (100 MHz, DMSO-d_6): δ 189.236, 171.557, 167.614, 167.166, 159.394, 157.759, 139.417, 137.595, 131.985, 129.547, 128.969, 124.654, 123.557, 123.432, 120.286, 115.690, 55.887, 55.649, 40.609, 30.847, 30.030, 29.449, 18.976.

*3.1.5.5 2-(2-((5-Acetyl-1-(4-methoxyphenyl)-4-methyl-1H-imidazole-2-yl)thio)acetamido)-5-iodobenzoic acid (**SB5**).* Off-white solid; yield 81%. IR (ν_{max}, cm^{-1}): 3674 (O–H), 1708–1680 (C=O), 1533, 1504 (amide II, N–H bending/C–N stretching), 1596–1504 (Ar C=C), 1438–1290, 1250–1005 (C–O/C–N), 837–694 (C–I), 942–626 (Ar C–H). MS (ESI) *m/z*: 566 $[M + H]^+$; ^{1}H NMR (400 MHz, DMSO-d_6) δ: 11.96 (s, 1H, COOH), 8.37 (d, J = 8.8 Hz, 1H, Ar–H), 8.24 (d, J = 2.0 Hz, 1H, Ar–H), 7.90 (dd, J = 8.8, 2.0 Hz, 1H, Ar–H), 7.56 (d, J = 8.8 Hz, 2H, Ar–H), 7.07 (d, J = 8.8 Hz, 2H, Ar–H), 4.71 (s, 2H, S–CH_2), 3.79 (s, 3H, OCH_3), 2.50 (s, 3H, $COCH_3$), 2.44 (s, 3H, CH_3); ^{13}C NMR (100 MHz, DMSO-d_6): δ 189.568, 171.854, 168.754, 167.603, 159.446, 157.512, 142.542, 140.430, 139.628, 137.428, 128.655, 124.345, 122.225, 115.822, 86.661, 57.238, 55.908, 40.555, 30.246, 29.993, 18.957.

*3.1.5.6 2-(2-((5-Acetyl-1-(4-methoxyphenyl)-4-methyl-1H-imidazole-2-yl)thio)acetamido)-4-nitrobenzoic acid (**SB6**).* Yellow solid; yield 80%. IR (ν_{max}, cm^{-1}): 3501–3426 (O–H/N–H stretching), 3125–3029 (Ar C–H), 2929, 2859 (aliphatic C–H), 1705–1660 (C=O), 1533 (amide II, N–H bending/C–N stretching), 1520 and 1345 (NO_2 asymmetric and symmetric stretching), 1475–1304 (Ar C=C), 1253–1026 (C–O/C–N), 956–692 (Ar C–H). MS (ESI) *m/z*: 485 $[M + H]^+$; ^{1}H NMR (400 MHz, DMSO-d_6) δ: 11.97 (s, 1H, COOH), 8.33 (d, $J = 8.8$ Hz, 1H, Ar–H), 8.22 (s, 1H, Ar–H), 7.87 (d, $J = 8.8$ Hz, 1H, Ar–H), 7.53 (d, $J = 7.6$ Hz, 2H, Ar–H), 7.05 (d, $J = 8.4$ Hz, 2H, Ar–H), 4.69 (s, 2H, S–CH_2), 3.77 (s, 3H, OCH_3), 2.51 (s, 3H, $COCH_3$), 2.43 (s, 3H, CH_3); ^{13}C NMR (100 MHz, DMSO-d_6): δ 189.897, 171.919, 167.509, 165.882, 159.435, 157.589, 142.455, 140.296, 139.634, 137.353, 128.827, 124.305, 122.300, 115.813, 86.622, 57.150, 55.888, 40.256, 29.882, 18.929.

*3.1.5.7 4-(2-((5-Acetyl-1-(4-methoxyphenyl)-4-methyl-1H-imidazole-2-yl)thio)acetamido)-2-fluorobenzoic acid (**SB7**).* White solid; yield 82%. IR (ν_{max}, cm^{-1}): 3342 (O–H/N–H stretching), 3125–3029 (Ar C–H), 2929, 2859 (aliphatic C–H), 1699, 1670 (C=O), 1510 (amide II, N–H bending/C–N stretching), 1419, 1377, 1341, 1303 (aromatic/skeletal vibrations), 1255–1104 (C–O/C–N stretching), 1169–976 (Ar–F stretching), 839, 761, 729, 694, 661, 613 (Ar C–H). MS (ESI) *m/z*: 458 $[M + H]^+$; ^{1}H NMR (400 MHz, DMSO-d_6) δ: 10.84 (s, 1H, COOH), 7.75 (d, $J = 8.8$ Hz, 1H, Ar–H), 7.55–749 (m, 3H, Ar–H), 7.33 (d, $J = 1.6$ Hz, 1H, Ar–H), 7.05 (d, $J = 9.2$ Hz, 2H, Ar–H), 4.73 (s, 2H, S–CH_2), 3.78 (s, 3H, OCH_3), 2.56 (s, 3H, $COCH_3$), 2.49 (s, 3H, CH_3); ^{13}C NMR (100 MHz, DMSO-d_6): δ 189.325, 171.511, 167.654, 160.371, 159.456, 157.793, 142.758, 137.512, 132.974, 128.978, 123.521, 115.764, 114.293, 106.971, 106.574, 55.948, 30.070, 19.026; ^{19}F NMR (376 MHz, DMSO-d_6): δ: −107.60 (s, 1F).

3.2 Biological activity

3.2.1 Antimicrobial evaluation. The antimicrobial activity of the synthesized compounds was evaluated at the Department of Microbiology, School of Sciences, Gujarat University, Ahmedabad, India, using a standard broth dilution method. Mueller–Hinton Broth (MHB) was employed for bacterial cultures, and the inoculum density for each organism was adjusted to approximately 10^6 CFU mL^{-1} using the 0.5 McFarland turbidity standard. Stock solutions of all synthesized compounds were prepared at a concentration of 2000 μg mL^{-1} in appropriate solvents, and serial dilutions were performed in MHB for MIC determination. For the sensitive MTCC strains, primary screening was performed using concentrations of 1000, 500, 250, and 125 μg mL^{-1}, and compounds exhibiting activity were subjected to secondary screening at 100, 50, 25, 12.5, and 6.25 μg mL^{-1}. For the resistant strains, an extended two-fold dilution series of 1024, 512, 256, 128, 64, 32, 16, 8, 4, and 2 μg mL^{-1} was used due to their higher resistance profiles. After inoculation, all tubes were incubated at 37 °C for 24 hours, and the minimum inhibitory concentration (MIC) was recorded as the lowest concentration of the compound where no visible bacterial growth after incubation. Control tubes without antibiotic were sub-cultured prior to incubation to verify the accuracy of the drug dilutions and organism viability.[16,17]

3.2.2 *In vitro* folate enzyme inhibition assay (DHPS/DHFR). *In vitro* enzyme assays for DHPS and DHFR are accomplished according to the reported procedures.[18,19]

3.2.3 Antioxidant activity. The DPPH radical scavenging assay was conducted according to Blois' 1958 protocol with minor adjustments. A 0.1 mM solution of DPPH was prepared in methanol. From this, 300 μL was mixed with the synthesized compounds at concentrations ranging from 15.62 to 1000 μg mL^{-1}. After vortexing and a 30-minute incubation at room temperature, methanol-DPPH served as the negative control, and ascorbic acid as the positive control. The assay was performed in triplicate to make sure the readings were consistent. The absorbance was measured at 520 nm using an EPOCH microplate spectrophotometer. The percentage scavenging was calculated using the formula $[(A_0 - A_1)/A_1] \times 100$, where A_0 is the control absorbance and A_1 is the sample absorbance. The results are expressed as mean ± SD and IC_{50} values determined for **SB2** concentrations.[20]

3.2.4 Cytotoxicity assay. The cytotoxicity study was carried out on the A549 and HEK293 cell line (from NCCS Pune) and was assessed using the MTT assay. The cells were cultured at a density of 10 000 cells per well in a 96-well plate and incubated in an air-jacketed CO_2 incubator at 37 °C, 5% CO_2 for 24 hours in DMEM (Dulbecco's Modified Eagle Medium-AL149-1L-HIMEDIA). The medium contained 10% FBS (Fetal Bovine Serum-HIMEDIA-RM 10432) and 1% antibiotic solution (Penicillin-Streptomycin-Sigma-Aldrich P0781). In preparing the sample, 1 mg of test compound was dissolved in DMSO to ensure solubility. After this, the solution was mixed with culture medium in a proportion of 1 : 99, where the culture and solution are mixed to prepare a stock solution. Further dilutions of this solution were made in the range of 15.625 μg mL^{-1} to 1000 μg mL^{-1}. Lastly, cells were seeded at 10 000 cells per well, with approximately 70–80% confluence desired by the end of treatment. After 24 hours, cells were exposed to samples at concentrations between 15.625 μg mL^{-1} and 1000 μg mL^{-1} for another 24 hours. Subsequently, 10 μL of 5 mg mL^{-1} 3-(4,5-dimethylthiazol-2-yl)-2,5-diphenyltetrazolium bromide (MTT, CCK003-HIMEDIA) was added to each well and incubated for 3 hours to develop formazan crystals. The supernatant was carefully removed, and the crystals were dissolved in 100 μL DMSO. Absorbance was measured at 570 nm using a microplate reader (Epoch, BioTek, USA). Cell viability (%) was calculated with the following formula.[21]

$$\text{Cell viability}(\%) = \frac{\text{Absorbance of treated cells}}{\text{Absorbance of control cells}} \times 100$$

3.2.4.1. Statistical analysis. A one-way ANOVA with repetitions was conducted using GraphPad Prism, Version 10. Results are shown as mean ± standard deviation. Significance levels are indicated as follows: *$p < 0.05$, **$p < 0.01$, ***$p < 0.001$, ****$p <$ 0.0001, and "ns" for non-significant results. Experiments were performed in triplicate to ensure reproducibility and reliability. The statistical analysis also included using Microsoft Excel and R (version 4.5.0), employing a one-way ANOVA with repeated measures.

3.2.5 *In vitro* DNA nicking study. The protective activity of the synthesized compounds against DNA damage was determined *via* an *in vitro* DNA nicking assay that involves a Fenton reaction. The plasmid DNA (pBR322) selected for this study is double-stranded and circular. The Fenton reagent was prepared by mixing 30 mM hydrogen peroxide (H_2O_2), 50 μM ascorbic acid, and 80 μM ferric chloride ($FeCl_3$). DNA was combined with 10 μl of samples and incubated at 37 °C for 60 and 120 minutes. Thereafter, 10 μl of the Fenton reagent was added. The mixture was incubated for the same duration. Subsequently, loading dye was added, and the mixture was electrophoresed on a 1.5% agarose gel at 80 V. The gel was then assessed and imaged with the BioDoc-it™ system from UVP.[22]

3.2.6 Spectroscopic studies of CT and HS DNA interaction with SB2. A uniform DNA solution was prepared using Herring Sperm DNA (HS-DNA, 33 μg mL^{-1}) and Calf Thymus DNA (CT-DNA, 50 μg mL^{-1}) in injection water, then stored at 5 °C for 24 hours to hydrate. DNA concentrations were measured with UV-vis spectrophotometry using $\varepsilon 260 = 6600\ cm^{-1}\ M^{-1}$. Absorption spectra from 200–800 nm were recorded in the absence and presence of test samples **SB2**.[23]

3.2.7 Chemical stability assay. Chemical stability of **SB2** was determined by HPLC under physiological conditions for 72 h at 37 °C. Samples were collected after a certain period, and analysis was performed using reverse-phase HPLC (C18 column). The results were based on the detection of retention time and peak area.

3.3 Computational studies

3.3.1 Molecular docking studies. Molecular docking studies were performed to investigate the binding modes of the synthesized compounds within the active sites of DHPS (PDB ID: 6CLV)[24] and DHFR (PDB ID: 6PBO),[25] key enzymes in the folate biosynthesis pathway. The crystal structures were retrieved from the RCSB Protein Data Bank and prepared using the Protein Preparation Wizard in Schrödinger by assigning bond orders, adding missing hydrogen atoms, optimizing hydrogen-bonding networks, and removing crystallographic water molecules beyond 5 Å from heteroatoms. The prepared proteins were subjected to restrained energy minimization using the OPLS4 force field. Ligand structures were prepared using the LigPrep module, where appropriate ionization states at physiological pH were generated and geometries were optimized to obtain low-energy conformations.[26] Receptor grids were generated by defining the active site region based on the co-crystallized ligands. Docking simulations were carried out using the Glide module in extra precision (XP) mode to predict binding conformations and affinities. The best binding poses were selected based on Glide scores and interaction profiles, and the resulting protein–ligand complexes were analyzed using Schrödinger Maestro.[27,28]

3.3.2 Molecular dynamics and free energy analysis. Molecular dynamics (MD) simulations were performed on the selected lead compounds to assess the protein-ligand complexes' stability and dynamic behaviour. Binding free energy calculations (MM-GBSA), principal component analysis (PCA), free energy landscape analysis (FEL), and dynamic cross-correlation matrix (DCCM) analyses were carried out using previously published methodologies.[29,30]

3.3.3 *In silico* toxicity and ADMET assessment. *In silico* toxicity and pharmacokinetic properties of the compounds **SB1–SB7** were evaluated using Schrödinger QikProp, Protox-II (version 3.0), and the SwissADME web tool. QikProp was employed to estimate key ADMET parameters, including lipophilicity, permeability, and absorption-related descriptors. Protox-II was used to predict toxicity endpoints such as LD_{50}, mutagenicity, and immunotoxicity. Additionally, SwissADME was utilized to assess pharmacokinetic behavior, including gastrointestinal absorption and blood–brain barrier permeability using the BOILED-Egg model.[31]

4. Result and discussion

4.1 Chemistry

The synthetic route to the target compounds **SB1–SB7** is illustrated in Scheme 1, with all derivatives presented in Table 1. The crucial intermediate, 1-(2-mercapto-1-(4-methoxyphenyl)-4-methyl-1*H*-imidazole-5-yl)ethan-1-one (**S**), was synthesized from *p*-methoxyaniline, 3-chloro-2,4-pentanedione, and potassium thiocyanate following a previously established protocol (Step 1).[14] Subsequently, derivatives of (2-chloroacetamido) benzoic acid **(B1–B7)** were synthesized from several PABA analogues and chloroacetyl chloride in MDC in the presence of TEA through a nucleophilic acyl substitution reaction (Step 2). The final compounds (**SB1–SB7**) were synthesized in high yields *via* the reaction of compound **S** with different substituted (2-chloroacetamido)benzoic acid derivatives in the presence of potassium carbonate in DMF under microwave irradiation (Step 3). Microwave conditions demonstrated superior efficiency compared to conventional reflux, resulting in shorter reaction times and lower catalyst usage.

Fig. S1 illustrates the reaction mechanism. A proposed mechanism is suggested for the synthesis of (2-((5-acetyl-1-(4-methoxyphenyl)-4-methyl-1*H*-imidazole-2-yl)thio)acetamido) benzoic acid derivatives with various substitution patterns on the benzoic acid ring. The synthesis of molecule **S** entails an SN^2 reaction between 3-chloro-2,4-pentanedione and *p*-methoxyaniline, succeeded by cyclization in the presence of ammonium thiocyanate *via* successive deammonification, dehydration, and proton transfer processes. In the reaction, the (2-chloroacetamido)benzoic acid derivatives (**B1–B7**) react with the thiol group of molecule **S** through a nucleophilic substitution reaction to yield the final **SB1–SB7** compounds, and the HCl produced in the reaction is neutralized using K_2CO_3. The high percentage yield further confirms that the reaction process works well with the diverse analogues. However, Microwave irradiation exhibited better yield and shorter reaction time.

4.2 Evaluation of biological activity

4.2.1 Antimicrobial activity

4.2.1.1 Antimicrobial activity result against susceptible bacterial strains. The synthesized compounds' antimicrobial activity was evaluated against two Gram-positive (*S. aureus* MTCC 96 and *S. pyogenes* MTCC 442) and two Gram-negative pathogens

Table 1 shows the final structure of compounds **SB1–SB7**, their respective yield, and their melting point (M.P.) °C

Compound	R_1-NH	Product	Reaction time (min.)	Yield (%)	M.P. (^{0}C)
SB1	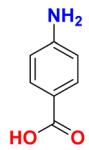	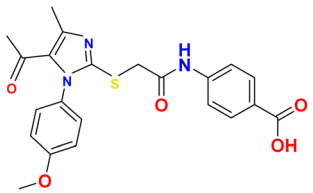	2.30	72	180
SB2	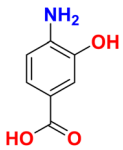	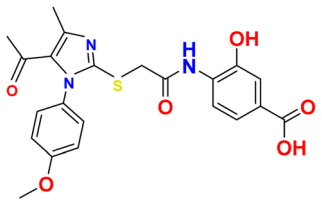	3.00	76	191
SB3	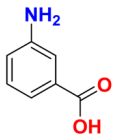	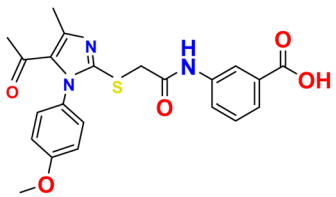	2.10	91	181
SB4	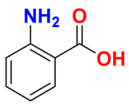	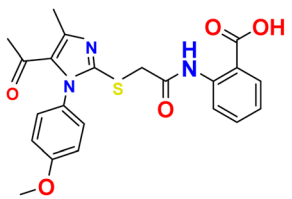	3.20	92	181
SB5	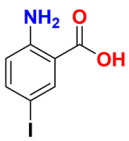	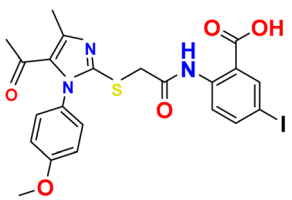	2.40	69	195
SB6	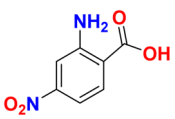	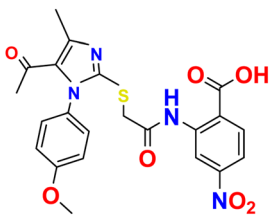	2.30	88	193
SB7	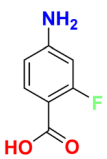	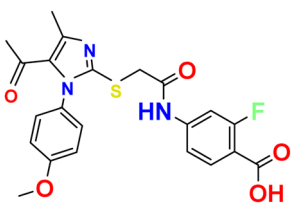	2.30	72	186

(*E. coli* MTCC 443 and *P. aeruginosa* MTCC 1688) using minimum inhibitory concentration (MIC) determination. The antimicrobial activity against susceptible strains suggests that the compounds **SB1–SB7** show broad-spectrum antimicrobial activity (Table 2). Among all the compounds, **SB2** demonstrates the most potent results, with very low MIC values against all the strains.

Table 2 Antimicrobial Activity Results against susceptible bacterial strains

Compound	*E. coli* MTCC 443 (μg mL^{-1})	*P.aeruginosa* MTCC 1688 (μg mL^{-1})	*S. aureus* MTCC 96 (μg mL^{-1})	*S. pyogenes* MTCC 442 (μg mL^{-1})
SB1	1	4	0.5	4
SB2	1	2	0.25	2
SB3	2	2	0.5	8
SB4	4	4	0.5	8
SB5	8	4	0.25	2
SB6	2	2	0.5	8
SB7	2	4	2	8
Norfloxacin	10	10	10	10
Ciprofloxacin	25	25	50	50
Gentamicin	1	1	0.25	0.5

The enhanced activity of **SB2** may be attributed to the presence of an *ortho*-hydroxyl group, which possibly enhances the hydrogen bonding. **SB5** indicated significant activity compared to standard drugs; hence, the iodine group is significant for the improved activity. **SB1** and **SB4** exhibited considerable antimicrobial activity against both the Gram-positive and Gram-negative strains, with MIC ranging from 0.5 to 4 μg mL^{-1}, revealing their broad spectrum. On the other hand, **SB4** and **SB6** were less efficient, with the inhibition of Gram-negative bacteria compared to the effective inhibition of Gram-positive bacteria. In contrast, **SB7** exhibited comparatively weak antimicrobial activity, especially against *S. aureus* and *S. pyogenes,* indicating a detrimental effect of fluoro substitution. The synthesized compounds demonstrated enhanced biological activity compared to standard drugs such as norfloxacin and ciprofloxacin.

Although Gentamicin exhibited superior antibacterial activity in certain cases, particularly against Gram-negative bacteria, its clinical utility is often limited by the rapid emergence of resistance.[32] In contrast, the synthesized compounds are designed to target the folate biosynthesis pathway through dual DHPS/DHFR inhibition, which is mechanistically distinct from aminoglycoside-mediated protein synthesis inhibition. This difference in mode of action is particularly relevant in the context of resistant strains such as MRSA, where reduced susceptibility to aminoglycosides has been widely reported.[33,34] Therefore, despite exhibiting slightly lower potency in some cases, the synthesized compounds offer a complementary therapeutic advantage by targeting alternative biochemical pathways, potentially reducing the likelihood of cross-resistance. These observations highlight the potential of the synthesized compounds for further optimization, particularly in the context of antimicrobial resistance, which was further evaluated against resistant bacterial strains.

4.2.1.2 Antimicrobial activity result against resistant strain. The potency of compounds **SB1–SB7** has been initially evaluated by employing the agar well diffusion method against MRSA and XDR *E. coli* at a concentration of 60 μg mL^{-1} (Table 3). Overall, all compounds exhibited potent inhibitory effects against MRSA and XDR *E. coli*, as evidenced by good inhibition zones. **SB2** showed the excellent inhibition of MRSA by producing a zone of 34 mm, followed by **SB5** (32 mm), **SB3**, and **SB4** (30 mm). While the standard drug combination trimethoprim–Sulfamethoxazole (TMP–SUL) showed 20 mm of zone inhibition. **SB7** exhibited the least inhibition of MRSA by producing an inhibition zone of 14 mm. Against XDR *E. coli*, compounds **SB1** and **SB2** exhibited notable inhibition zones of 26 mm and 24 mm, respectively, as compared to the standard drug amoxicillin, the inhibition zone of which was only 20 mm. **SB3**, **SB5**, and **SB6** compounds showed moderate inhibition, whereas **SB4** and **SB7** resulted in comparatively lower inhibition against XDR *E. coli*.

To quantitatively confirm their antimicrobial efficacy, the broth dilution method has been employed to evaluate MIC value of compounds **SB1–SB7** (Table 4). Consistent with the

Table 3 Zone of inhibition (mm) of synthesized compounds (SB1–SB7) against resistant bacterial strains (MRSA and XDR *E. coli*)[a]

Compound	MRSA (mm)	XDR *E. coli* (mm)
SB1	28	26
SB2	34	24
SB3	30	18
SB4	30	10
SB5	32	16
SB6	30	14
SB7	14	8
TMP–SUL	20	NT
Amoxicillin	NT	20

[a] NT means not tested. TMP–SUL: trimethoprim–Sulfamethoxazole combination.

Table 4 Antimicrobial activity results against resistant strains by dilution method (MIC)

Compound	MRSA (μg mL^{-1})	XDR *E. coli* (μg mL^{-1})
SB1	4	8
SB2	2	8
SB3	4	16
SB4	4	32
SB5	2	16
SB6	4	16
SB7	16	64
TMP–SUL	8	NT
Amoxicillin	NT	16

zone of inhibition results, **SB2** exhibited superior activity against MRSA, with an MIC value of 2 μg mL^{-1}, which is four times lower than the MIC of the standard drug combination TMP–SUL (8 μg mL^{-1}). **SB5** also showed an MIC value of 2 μg mL^{-1} against MRSA. The other compounds, **SB1**, **SB3**, **SB4**, and **SB6**, had MIC values of 4 μg mL^{-1}, which indicates substantial antimicrobial activity. For XDR *E. coli*, compounds **SB1** and **SB2** showed an MIC value of 8 μg mL^{-1}, demonstrating stronger activity than amoxicillin. Compounds **SB3**, **SB5**, and **SB6** showed moderate activity with an MIC value of 16 μg mL^{-1}, whereas compounds **SB4** and **SB7** were less effective with MIC values of 32 μg mL^{-1} and 64 μg mL^{-1}, respectively. The consistency demonstrated between the zone of inhibition and the MIC values confirms the antimicrobial test's reliability. All the antimicrobial assays were performed in triplicates, and the results were reproducible with consistent MIC values. The results demonstrate that the synthesized compounds were more effective against MRSA than XDR *E. coli*, with **SB2** being the most effective because of its superior antimicrobial activity.

Considering the above results, **SB2**, **SB5**, and **SB6** were selected for further evaluation of the folate pathway enzyme inhibition assay. **SB2** demonstrated the best MIC value against both MRSA and XDR *E. coli*. Similarly, **SB5** showed significant activity against MRSA. Although **SB6** demonstrated lower activity compared to **SB2** and **SB5**, it was selected for further enzyme inhibition assays because its maintained activity and distinct substitution pattern strengthen the structure–activity relationship (SAR) analysis. It is notable that antimicrobial effectiveness depends on factors beyond enzyme inhibition. Other factors, like membrane permeability and efflux, also have a crucial effect. The strength and structural difference in **SB2**, **SB5**, and **SB6** compounds are significant reasons for their selection for the further evaluation of the DHPS/DHFR enzyme binding assay.

Table 5 IC_{50} values for compounds **SB2**, **SB5**, and **SB6** against DHPS and DHFR enzymes with SUL and TMP as reference drugs

Compound	IC_{50} (DHPS, μg mL^{-1})[a]	IC_{50} (DHFR, μg mL^{-1})[a]
SB2	0.098 ± 0.005	1.218 ± 0.049
SB5	0.328 ± 0.017	0.622 ± 0.025
SB6	1.306 ± 0.068	2.721 ± 0.109
SUL	0.104 ± 0.005	NT
TMP	NT	0.337 ± 0.016

[a] The data are expressed as the mean ± SD of three independent experiments.

4.2.2 *In vitro* enzyme assay for DHPS and DHFR. *In vitro* enzyme inhibition studies against DHPS and DHFR were carried out to assess the inhibitory profiles of the most active candidates, with particular emphasis on compounds **SB2**, **SB5**, and **SB6**. The assays were performed using a DHPS catalytic assay and a DHFR inhibitor screening kit, with SUL and TMP employed as reference inhibitors for DHPS and DHFR, respectively. The half-maximal inhibitory concentration (IC_{50}) values were determined for each test compound and standard and are summarized in Table 5 (and depicted in Fig. 2), enabling a direct comparison of their relative potencies toward both targets.

The IC_{50} data demonstrate that compound **SB2** is the most potent DHPS inhibitor in this series, exhibiting an IC_{50} of 0.098 ± 0.005 μg mL^{-1}, which is slightly superior to SUL (IC_{50} = 0.104 ± 0.005 μg mL^{-1}). This enhancement in DHPS inhibition suggests a favorable contribution of the diazole-linked *S*-acetamido substituent at the *para*-position of the benzene carboxylic acid scaffold to target engagement at the DHPS active site. In contrast, **SB2** displays only modest activity against DHFR, with an IC_{50} of 1.218 ± 0.049 μg mL^{-1}, indicating a clear preference of this scaffold for DHPS over DHFR and highlighting its DHPS-selective profile.

Compound **SB5** shows complementary behavior. It significantly inhibits DHFR with an IC_{50} of 0.622 ± 0.025 μg mL^{-1}, which is approximately half the potency of TMP (IC_{50} = 0.337 ± 0.016 μg mL^{-1}). At the same time, it retains moderate DHPS inhibition (IC_{50} = 0.328 ± 0.017 μg mL^{-1}). The presence of the

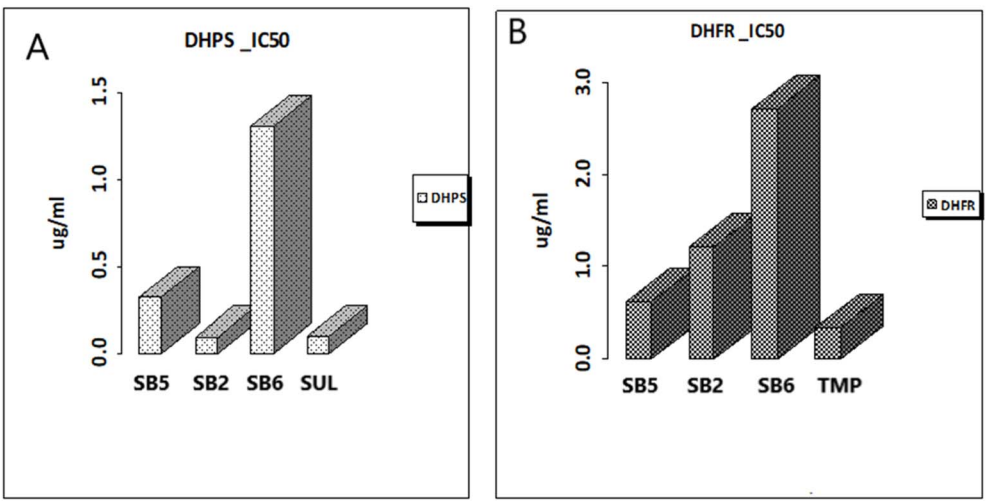

Fig. 2 Inhibition of the efficacy of the compounds toward (A) DHPS enzyme and (B) DHFR enzyme.

o-acetamido benzene carboxylic acid core combined with a *para*-iodo substituent appears to be beneficial DHFR binding. This likely improves hydrophobic and/or halogen-bonding interactions within the DHFR active site, which is evident in the IC_{50} value. This dual, though DHFR-oriented, activity, positions **SB5** as a promising DHFR biased inhibitor with ancillary DHPS inhibition, which could be advantageous in reducing the emergence of resistance through partial multi-target engagement.

Within the same series, **SB6** was clearly less active than **SB2** and **SB5** at both enzyme targets, with IC_{50} values of 1.306 ± 0.068 μg mL^{-1} for DHPS and 2.721 ± 0.109 μg mL^{-1} for DHFR, underscoring the critical role of the specific substitution patterns present in **SB2** and **SB5** for optimal enzyme inhibition. The inferior performance of **SB6** suggests that its structural features of the nitro group containing PABA scaffold do not adequately complement the binding environments of either DHPS or DHFR, thereby reinforcing the structure–activity relationship trends inferred from **SB2** and **SB5**. These observations collectively emphasize that fine-tuning the acetamido substitution (position and nature) and the electronic properties of the aromatic ring (*e.g.*, iodo *versus* other substituents) is essential for achieving high potency and selectivity toward the folate pathway enzymes.

Taken together, the markedly improved DHPS inhibition of **SB2** relative to SUL, combined with the significant DHFR inhibitory activity of **SB5** compared to TMP, supports the view that these two compounds could act as complementary inhibitors within the folate biosynthetic pathway (Fig. 3). **SB2** emerges as a DHPS-preferring inhibitor with potency comparable to, and slightly better than, the standard sulfonamide, whereas **SB5** behaves as a DHFR-oriented analog with relevant residual DHPS activity, mimicking in part the dual-target strategy of the SUL–TMP combination. Consequently, **SB2** and **SB5** can be considered promising lead candidates for further optimization as potential antibacterial agents, either as standalone molecules or in a rationally designed combination regimen aimed at simultaneous or sequential blockade of DHPS and DHFR.

4.2.3 Antioxidant activity results. The DPPH radical-scavenging assay results indicated that both ascorbic acid and **SB2** exhibited antioxidant properties throughout the evaluated concentration spectrum, specifically from 15.62 to 1000 μg mL^{-1}. Ascorbic acid demonstrated a consistently high scavenging efficiency; it maintained over 50% activity at the lowest concentration and achieved approximately 75–80% at elevated doses, as illustrated in Fig. 4. **SB2** exhibited pronounced antioxidant properties, as evidenced by a consistent, concentration-dependent enhancement in scavenging capacity. Specifically, the activity increased from about 12% at a concentration of 15.62 μg mL^{-1} to roughly 55% at 1000 μg mL^{-1}.

This gradual increase suggests that **SB2** interacts with DPPH radicals, which strengthens its antioxidant effect as the dosage increases. The calculated IC_{50} values corroborate this finding; specifically, **SB2** exhibited an IC_{50} of 749.6 ± 50.1 μg mL^{-1}, whereas ascorbic acid demonstrated a considerably lower IC_{50} of 14.08 ± 0.63 μg mL^{-1}, which is consistent with its established potent antioxidant capacity. Statistical analysis showed highly significant differences between ascorbic acid and **SB2** at all concentrations (****, $p < 0.0001$). The small error bars in the data suggest that the results are both reproducible and reliable. The DPPH assay is used to measure a compound's ability to donate electrons or hydrogen atoms, which helps to neutralize free radicals. The pronounced efficacy of ascorbic acid aligns with its swift electron-donating characteristics. In contrast, the progressive enhancement seen with **SB2** suggests the presence

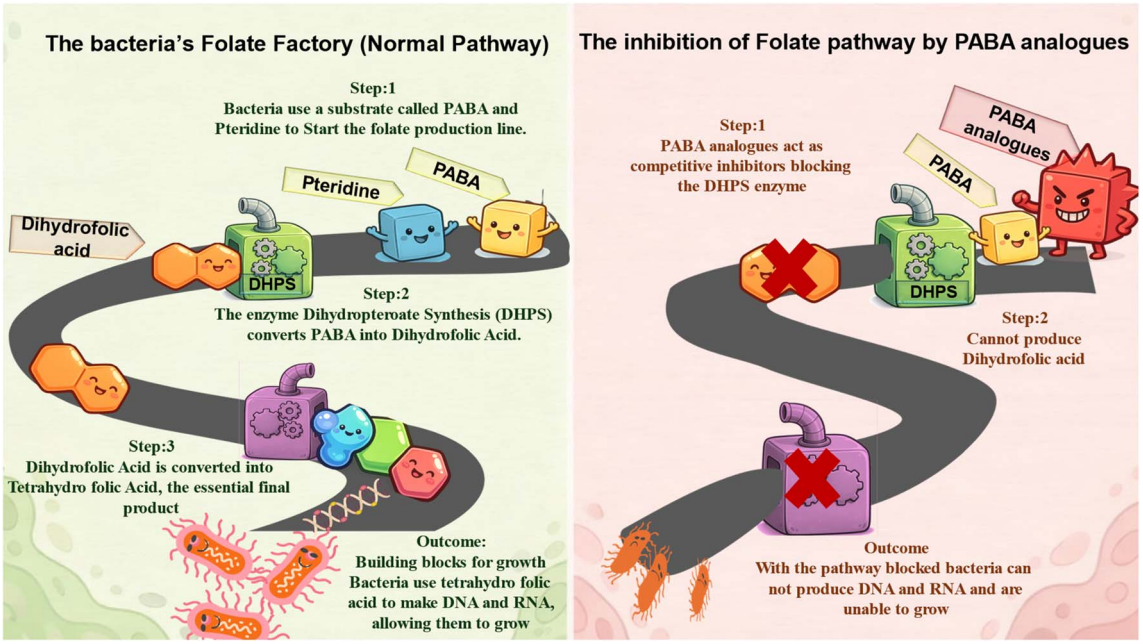

Fig. 3 Illustrates the normal bacterial folate pathway and the blocked folate pathway caused by PABA analogues.

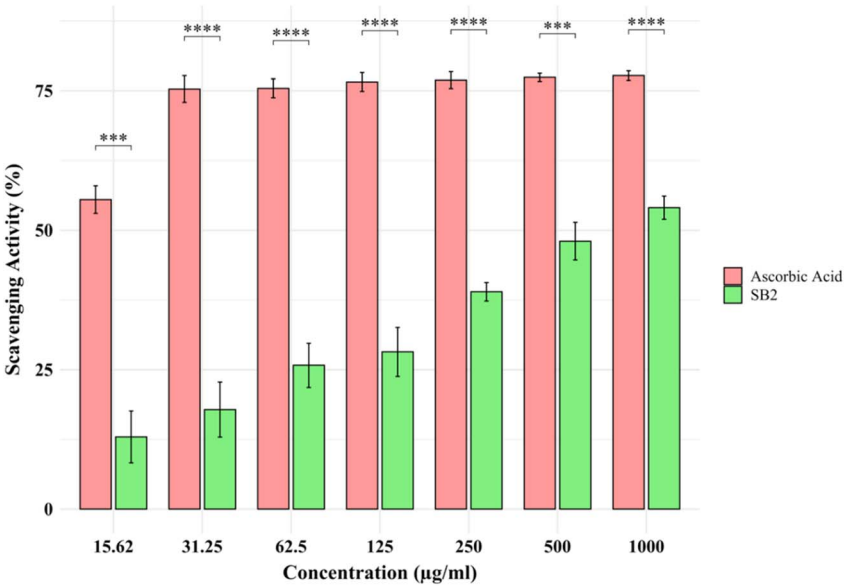

Fig. 4 DPPH radical scavenging activity of **SB2**.

of functional groups that interact effectively with radicals. This interaction supports a more stable and lasting radical-quenching effect. Although **SB2** required higher concentrations to show a moderate scavenging effect, its consistent dose–response relationship suggests it could be used to control antioxidant activity.

This type of response can be advantageous in biological systems, where a prolonged antioxidant effect helps maintain redox balance, rather than causing a quick, short-lived burst of activity. Antioxidants are crucial in living organisms for limiting oxidative stress caused by reactive oxygen species (ROS), such as hydroxyl, superoxide, and peroxyl radicals.[35] The observed dose-dependent scavenging activity of **SB2** suggests that it can make

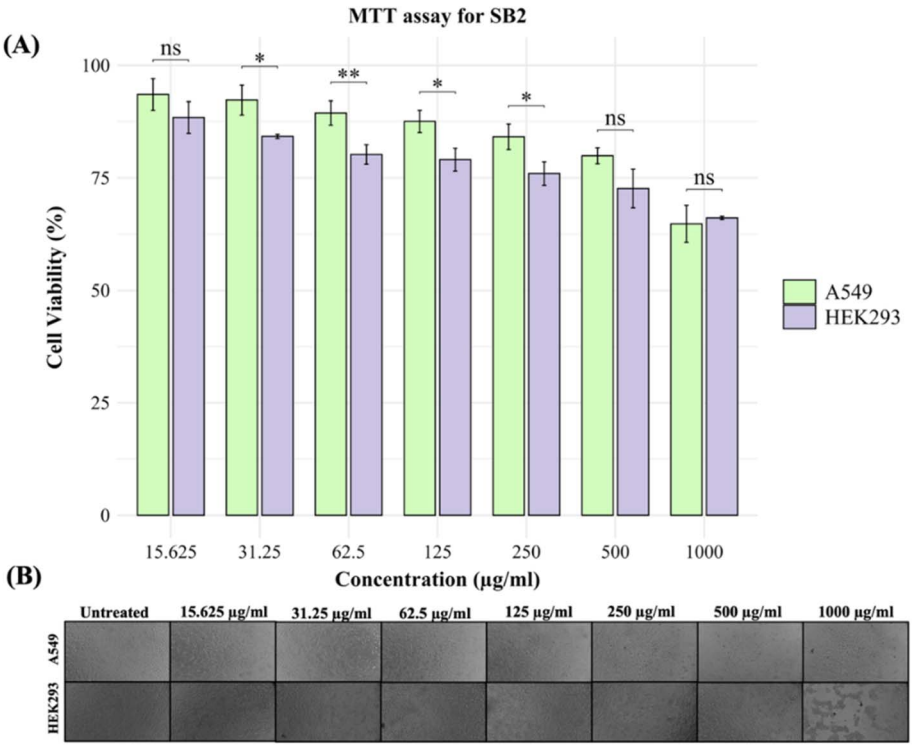

Fig. 5 % Cell viability graph of **SB2** on (A) A549 and HEK293 cell lines and (B) microscopic images (100×) showing morphological changes in treated cells.

a meaningful contribution to free radical neutralization, especially when present at sufficient levels or in combination with other bioactive compounds. The data suggest that **SB2** has significant antioxidant properties, depending on the amount used. This supports its potential as a functional radical-scavenging agent, comparable to established standards like ascorbic acid.

4.2.4 Cytotoxicity results. The cytotoxic effects of **SB2** were evaluated using the MTT assay in both A549 (lung cancer) and HEK293 (non-cancerous human embryonic kidney) cell lines across a concentration range of 15.625 to 1000 μg mL^{-1} (Fig. 5A). A gradual, concentration-dependent decline in cell viability was observed in both cell lines. However, A549 cells consistently exhibited slightly higher viability compared to HEK293 cells at most concentrations, indicating a marginally greater sensitivity of HEK293 cells toward **SB2**. At lower concentrations (15.625–125 μg mL^{-1}), both cell lines maintained high viability (>85–95%), suggesting minimal cytotoxic effects in this range. As the concentration increased to 250 and 500 μg mL^{-1}, a moderate reduction in viability was observed, with A549 cells retaining approximately 80–85% viability and HEK293 cells showing slightly lower values (∼75–80%). At the highest concentration (1000 μg mL^{-1}), cell viability decreased more noticeably, reaching approximately 60–65% in A549 and ∼65–70% in HEK293 cells. Despite this reduction, a substantial proportion of cells remained viable, indicating the absence of acute cytotoxicity. Statistical analysis (denoted by ns, *, and **) revealed that most differences between the two cell lines were either non-significant or moderately significant at specific concentrations, supporting a consistent but mild cytotoxic response. Importantly, the IC_{50} value was not achieved within the tested concentration range for either cell line, suggesting that the IC_{50} of **SB2** exceeds 1000 μg mL^{-1}. Further increases in concentration were limited by solubility constraints and the risk of solvent-induced cytotoxicity, which could interfere with assay accuracy.

Microscopic observations (Fig. 5B) corroborated the MTT results. Both A549 and HEK293 cells maintained normal morphology at lower concentrations, with intact cell structure and adherence. At higher concentrations (≥500 μg mL^{-1}), slight morphological alterations such as reduced cell density, mild shrinkage, and partial detachment were observed, but no extensive cell lysis or severe damage was evident. The MTT assay reflects mitochondrial metabolic activity, and the sustained viability of both cell lines suggests that **SB2** does not significantly impair cellular metabolism or induce substantial cell death under the tested conditions. Overall, these findings indicate that **SB2** exhibits good biocompatibility toward both cancerous and non-cancerous mammalian cells. The relatively low cytotoxicity, combined with previously observed biological activities, suggests that **SB2** may exert selective effects, potentially acting through non-genotoxic or redox-mediated mechanisms. This selective and mild action supports its potential as a safe bioactive compound, particularly in applications where minimal host cell toxicity is desirable.

4.2.5 DNA nicking results. The DNA nicking assay was employed to evaluate the effect of **SB2** on plasmid DNA under oxidative conditions. (lane 2) The untreated pBR322 plasmid exhibited a predominant supercoiled Form I, confirming structural integrity (Fig. 6). Incubation with **SB2** alone for 60 and 120 min (lanes 3 and 6) preserved the supercoiled DNA was maintained without detectable conversion to nicked (Form II) or linear (Form III) DNA, indicating that **SB2** does not induce direct DNA cleavage under the studied conditions. In contrast, treatment with Fenton's reagent (lanes 4 and 8) resulted in formation of open circular and linear DNA along with noticeable degradation upon prolonged exposure, consistent with hydroxyl radical-induced strand breakage. Notably, co-treatment with **SB2** (Lanes 5 and 7) resulted in greater retention of the supercoiled form and reduced formation of damaged DNA species compared to the Fenton-only samples, indicating mitigation of oxidative DNA damage. These observations suggest that **SB2** does not act through nonspecific DNA cleavage but may influence oxidative processes. This behavior is consistent with compounds that induce controlled oxidative stress to microbial systems, without causing significant DNA damage to the host.

The MTT assay results demonstrated high cell viability in A549 cells, indicating good biocompatibility of **SB2** under the tested conditions. These findings support its favourable safety profile and are consistent with its non-destructive interaction with DNA.[36] Notably, the observed DNA protective effect, together with maintained antimicrobial activity, indicates that **SB2** can exert its biological effects without inducing unintended damage to the host genetic material. Mechanistically, these findings support the possibility that **SB2** operates through redox modulation or enzyme-targeted pathways, rather than nonspecific DNA disruption. Taken together, these findings suggest that **SB2** interacts with DNA in non-destructive manner and

Fig. 6 Gel interaction of pBR322 DNA **SB2**. Lane 1: 1 kb DNA ladder; lane 2: control pBR322; lane 3: pBR322 + **SB2** (37 °C for 60 min); lane 4: pBR322 + Fenton's reagent (37 °C for 60 min); lane 5: pBR322 + Fenton's reagent + **SB2** (37 °C for 60 min); lane 6: pBR322 + **SB2** (37 °C for 120 min); lane 7: pBR322 + Fenton's reagent (37 °C for 120 min); lane 8: pBR322 + Fenton's reagent + **SB2** (37 °C for 120 min).

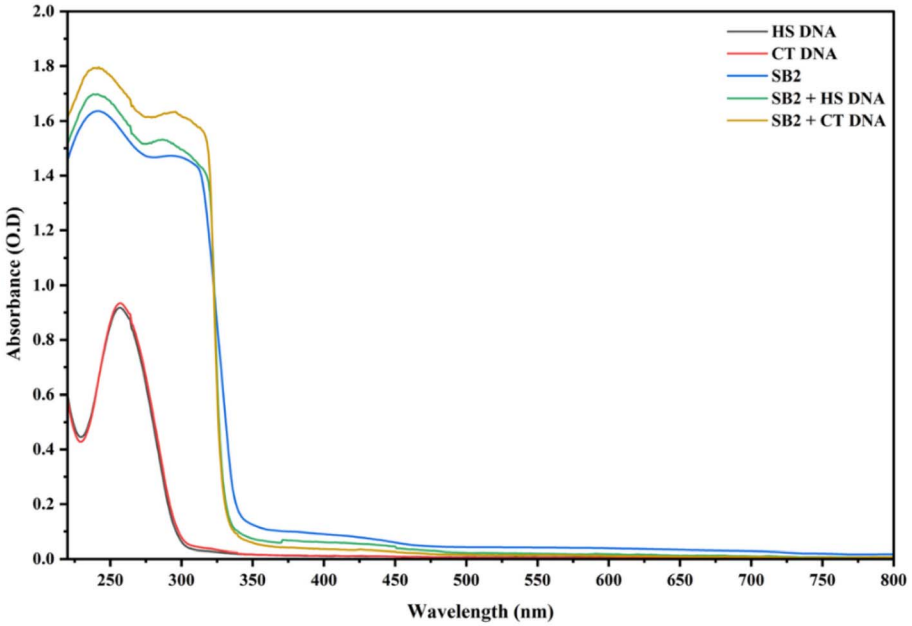

Fig. 7 UV-visible absorption spectra illustrating the interaction of SB2 with calf thymus (CT) DNA and herring sperm (HS) DNA.

support its potential as a biologically active compound with a favourable safety profile.[37]

4.2.6 Spectroscopic studies of CT and HS DNA interaction. The interaction of SB2 with calf thymus (CT) DNA and herring sperm (HS) DNA was investigated using UV-visible absorption spectroscopy (Fig. 7). Both CT DNA and HS DNA exhibited a characteristic absorption band around ~260 nm, attributed to the $\pi \rightarrow \pi^*$ transitions of nucleotide bases. Upon addition of **SB2** to DNA, notable changes in the absorption spectra were observed. Specifically, an increase in absorbance intensity (hyperchromic effect) along with a slight shift in wavelength was detected in both CT DNA and HS DNA systems. These spectral variations indicate an interaction between **SB2** and DNA molecules, leading to perturbations in the DNA base-stacking environment.

The presence of hyperchromism suggests partial unwinding or loosening of the DNA double helix, thereby increasing the exposure of nucleobases and enhancing electronic transitions. However, the absence of strong hypochromism and significant bathochromic shift features typically associated with classical intercalative binding indicates that **SB2** does not strongly intercalate between DNA base pairs. Instead, the interaction is more likely mediated through groove binding or electrostatic interactions with the DNA backbone. Interestingly, similar spectral behavior was observed for both CT DNA and HS DNA, suggesting that **SB2** exhibits a comparable binding affinity toward different DNA sources without pronounced selectivity. The minor spectral shift further supports the formation of a **SB2**-DNA complex, confirming the binding capability of the compound. Importantly, when these findings are correlated with the DNA nicking assay results, **SB2** did not induce DNA strand cleavage but instead demonstrated a protective effect against Fenton reagent-induced oxidative damage. This indicates that although **SB2** interacts with DNA, it does not destabilize the genetic material in a damaging manner. Rather, the interaction appears to be non-destructive and potentially stabilizing, likely contributing to its observed DNA protective activity.

Overall, the spectroscopic analysis confirms that **SB2** binds to DNA through a non-intercalative mode, and this interaction, combined with its antioxidant properties, may play a crucial role in protecting DNA from oxidative stress. These findings highlight the non-genotoxic and potentially therapeutic nature of **SB2**.

4.2.7 Chemical stability assay. The chemical stability of **SB2** was evaluated by HPLC under physiological conditions over 72 h. The chromatographic profiles showed no significant variation in retention time (9.396–9.481 min), while the peak area remained essentially constant (99.93%). Moreover, no additional peaks or increase in impurity levels were observed, indicating the absence of detectable degradation (Fig. 8). The minor variations observed are attributed to routine instrumental fluctuations rather than chemical instability. Collectively, these results confirm that **SB2** maintains its structural integrity under the studied conditions. Together, these data provide evidence that the compounds remain stable in the studied environment. We agree that future stability studies will be performed using other methods of analysis to validate our findings.

4.3 Computational studies

4.3.1 Molecular docking. Molecular docking studies were performed to evaluate the binding affinity of the compounds toward DHPS (PDB ID: 6CLV) and DHFR (PDB ID: 6PBO). All compounds showed stronger binding affinity to the DHPS target and are better than the standard drugs SUL and

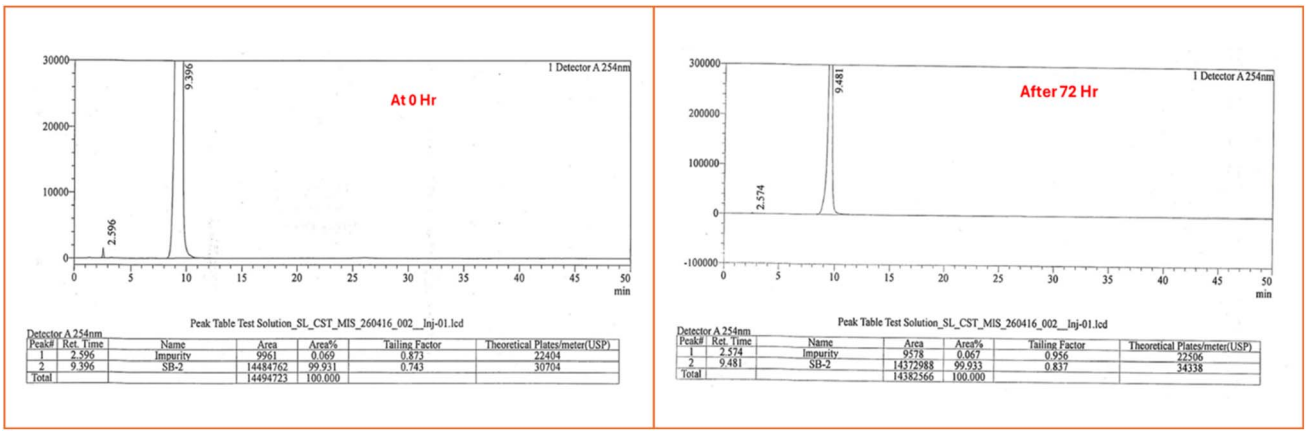

Fig. 8 HPLC chromatograms of **SB2** recorded at 0 h and after 72 h under physiological conditions, showing consistent retention time and no appearance of additional peaks, indicating the stability of the compound over the studied period.

sulfadiazine (SD), indicating improved binding with the PABA binding pocket of the DHPS enzyme (Table 6). The **SB2** compound showed a docking score of −6.376 kcal mol^{-1}, which is better than sulfamethoxazole (−2.489 kcal mol^{-1}) and sulfadiazine (−2.791 kcal mol^{-1}), followed by **SB6** (−5.902 kcal mol^{-1}) and **SB5** (−5.492 kcal mol^{-1}). Docking against DHFR revealed that all compounds showed potent binding affinity, which was quite comparable to that of the standard DHFR inhibitor trimethoprim (TMP) with a docking score of −8.469 kcal mol^{-1}. **SB2** exhibited a docking score of −8.187 kcal mol^{-1}, followed by **SB3** (−7.820 kcal mol^{-1}) and **SB6** (−7.361 kcal mol^{-1}), indicating favourable binding within the DHFR binding pocket. These results indicate that these compounds show dual binding potential toward both DHPS and DHFR. **SB2** emerges as the most promising candidate based on docking performance.

To further elucidate the binding mode and residue-level interactions, binding interactions of **SB2** compared to the reference drug SUL were analysed (Fig. 9a–d). **SB2** demonstrated stable polar and electrostatic interactions within the DHPS active site (PDB ID: 6CLV), including hydrogen bonds with ARG52 and ARG204, a water-mediated interaction with ASP15, and a π-cation interaction with LYS203. Hydrophobic interaction with PRO53 and the presence of oxygen-containing functional groups further supported effective binding within the active-site. In contrast, SUL had a greater interaction network, introducing several hydrogen bonds and salt bridges with residues such as ARG176, GLU179, ARG204, and LYS203 and hydrophobic and aromatic interactions with PHE205 and PRO53. Water-mediated interactions additionally assisted to stabilize the SUL–DHPS complex.[38] While SUL formed more interactions, **SB2** showed well defined electrostatic and aromatic contacts, suggesting a stable binding orientation within the active site.

Table 6 Docking score of compounds **SB1–SB7**

Compound	DHPS XPGscore (kcal mol^{-1})	DHFR XPGscore (kcal mol^{-1})
SB1	−5.246	−6.670
SB2	−6.376	−8.187
SB3	−4.414	−7.820
SB4	−4.799	−6.673
SB5	−5.492	−6.815
SB6	−5.902	−7.361
SB7	−5.057	−6.172
Sulfamethoxazole	−2.489	NT
Sulfadiazine	−2.791	NT
Trimethoprim	NT	−8.469

A similar interaction pattern was observed for the DHFR system (Fig. 10a–d) **SB5** exhibited a clear and stable binding orientation in the active site, supported by a network of polar, electrostatic, and water-mediated interactions. **SB5**-DHFR complex involved hydrogen bonding and ionic interaction with residues such as LYS45, THR46, SER49, ASN18, and ASP120. In addition, hydrophobic interactions between PHE92 and LEU20 contributed to ligand anchoring **SB5** within the binding pocket, enhancing steric interactions.[39] The oxygen-containing functional group in the **SB5** further facilitated direct hydrogen bonding and polar interaction, effectively binding the ligand within the DHFR active site. On the other hand, TMP showed a more rigid and targeted interaction pattern in the DHFR binding pocket. The TMP formed a salt bridge and hydrogen bond with ASP27, which resulted in strong electrostatic interactions. Additional hydrophobic interactions with residues such as LEU24, LEU54, PHE92, and ILE50 further supported ligand binding. However, TMP exhibited comparatively fewer water-mediated interactions than **SB5**, indicating a more direct but less adaptable interaction mode.

To further evaluate the dynamic behavior and interaction persistence of the docked complexes, molecular dynamics simulations were performed. Based on antimicrobial activity, the enzyme inhibition assay, and docking results, **SB2** and **SB5** were selected for detailed Molecular dynamic simulation analysis. Trajectories were analyzed using structural deviation and flexibility metrics (RMSD/RMSF) to examine conformational stability. Binding affinities were evaluated by using MM-GBSA,

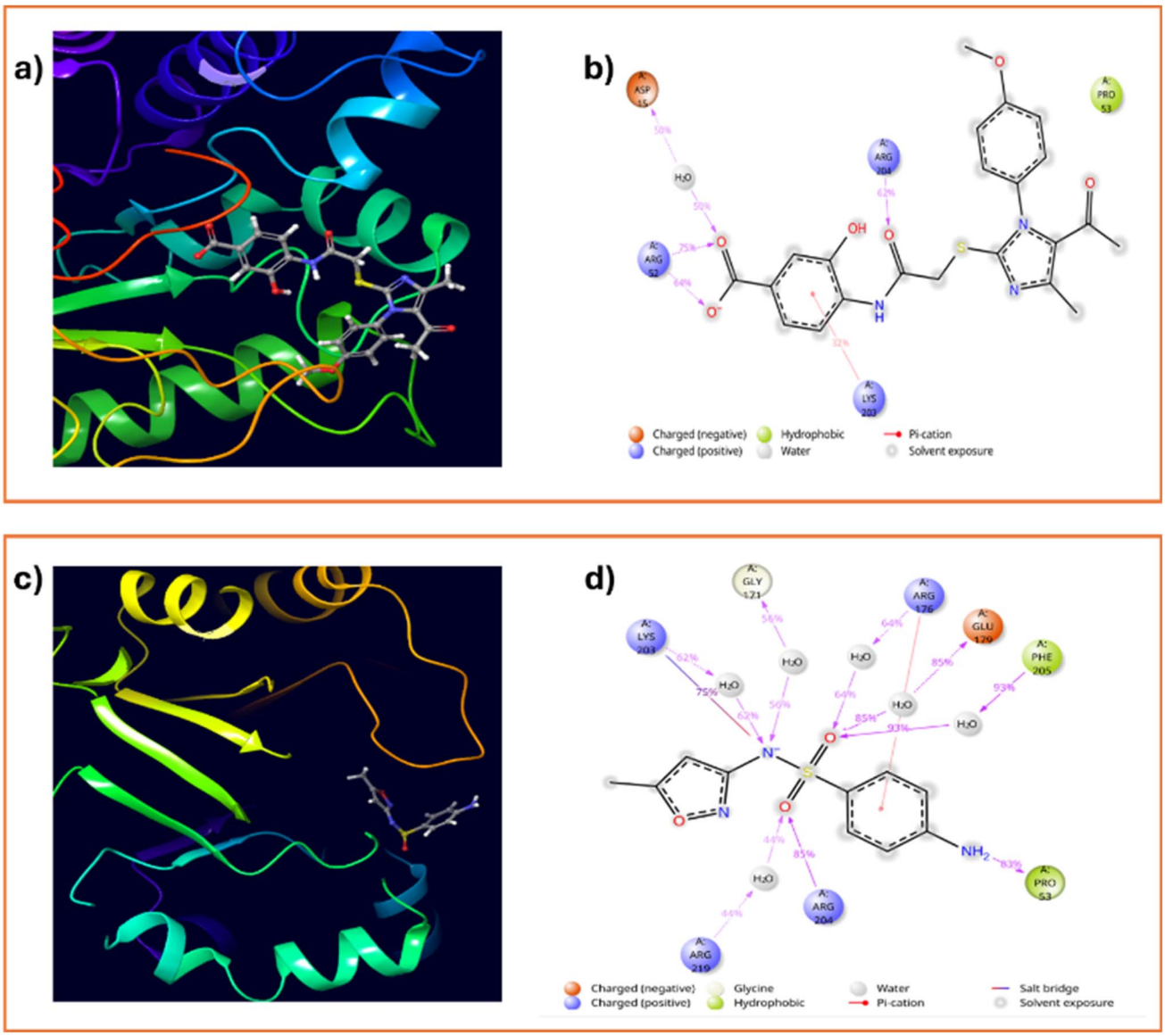

Fig. 9 (a) 3D docking pose of **SB2** within the DHPS active site (PDB ID: 6CLV). (b) 2D interaction of **SB2** showing hydrogen-bonding and hydrophobic contacts with active-site residues.(c) 3D pose of SUL within the DHPS active site (d) 2D interaction of SUL showing hydrogen bonding and hydrophobic contacts with active-site residues.

whereas global conformational stability was studied through FEL analysis. The dominant protein movements and ligand-induced dynamic effects were determined using PCA and DCCM, respectively.

The dynamic behaviour of the **SB2**-DHPS and SUL-DHPS complexes was evaluated using 100 ns MD simulations, and the resulting trajectories were analysed using RMSD, RMSF, and protein-ligand interaction profiling (Fig. 11a and b). The RMSD profile analysis of the **SB2**-DHPS complex demonstrated stable ligand positioning with low RMSD values (1.0–2.0 Å), indicating consistent accommodation within the active site. In contrast SUL-DHPS complex exhibited higher ligand RMSD fluctuations (2.0–2.5 Å) with notable oscillations, suggesting increased ligand mobility within the binding pocket. Despite this, the protein backbone remained stable in both systems.

4.3.2 Molecular dynamics and free energy analysis

4.3.2.1 Molecular dynamic stability and free energy analysis of DHPS complexes

4.3.2.1.1. RMSD and RMSF analysis. RMSF analysis further supported these observations. The **SB2**-DHPS complex exhibited lower residue fluctuations, with most values below 1.5 Å, particularly in the catalytic region. Residues near the active site showed reduced flexibility, indicating stable ligand accommodation. In contrast, the SUL-DHPS complex displayed higher fluctuations in regions adjacent to the active site, especially within loop regions, reflecting greater conformational flexibility.

4.3.2.1.2. Protein–ligand interaction analysis. The interaction fraction analysis further revealed significant differences in

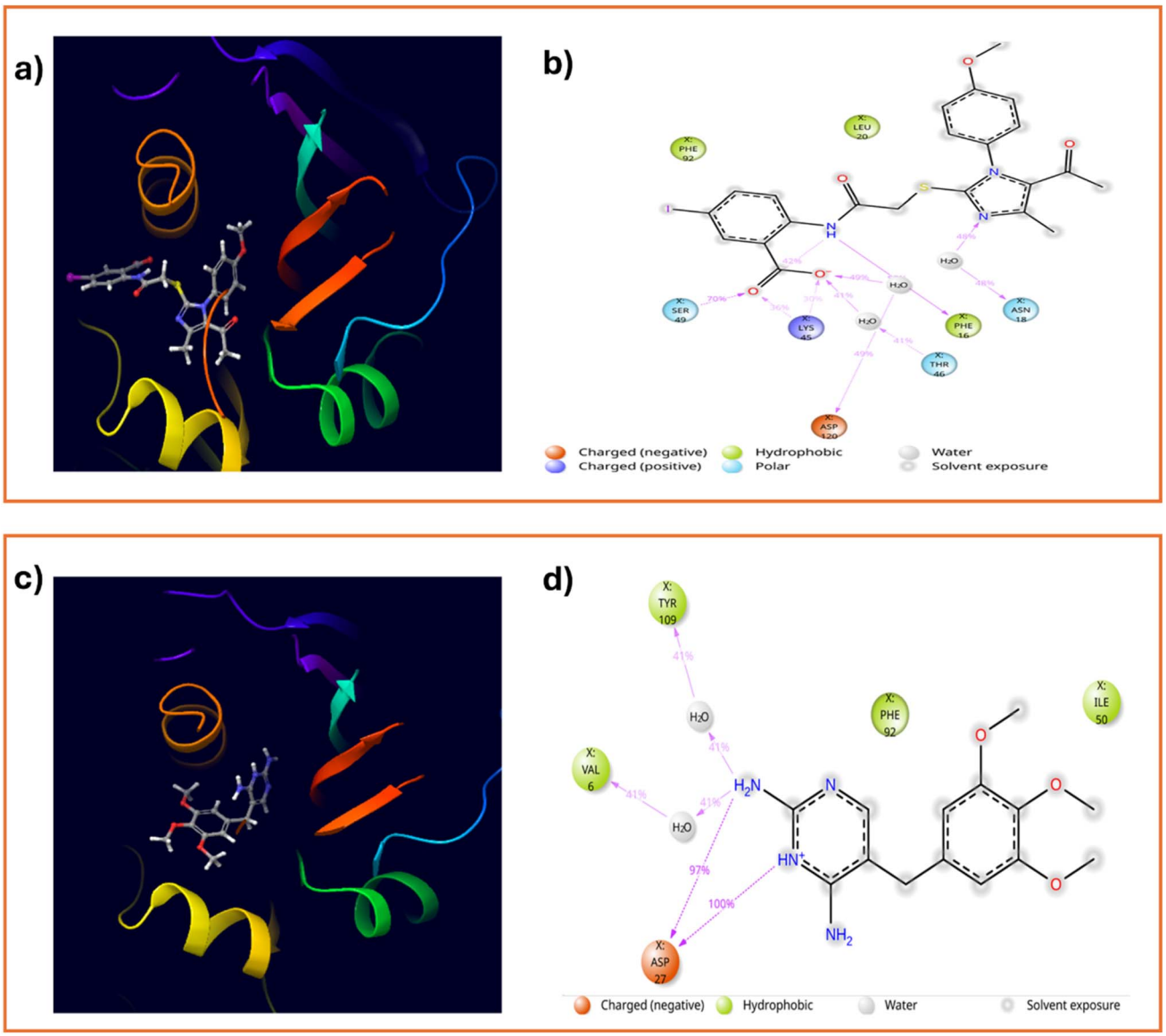

Fig. 10 (a) 3D docking pose of **SB5** within the DHFR active site (PDB ID: 6PBO). (b) 2D interaction of **SB5** showing hydrogen bonding and hydrophobic contacts with active-site residues. (c) 3D pose of TMP within the DHPS active site (d) 2D interaction of TMP showing hydrogen bonding and hydrophobic contacts with active-site residues.

binding engagement between the **SB2** and SUL (Fig. 12a and b). The **SB2**-DHPS complex has a robust interaction pattern that includes many hydrogen bonds, ionic interactions, hydrophobic contacts, and water bridges with key residues such as ARG176, GLU179, ARG204, and LYS203. This interaction showed a high occupancy and persisted throughout the simulation, indicating strong and sustained stability. In contrast, the interaction pattern of SUL-DHPS was less stable. It consisted mostly of transient hydrogen bonds and water-mediated contacts, as well as less frequent and weaker ionic interactions.[40] This resulted in a higher fluctuation and lower contact density compared to **SB2**, revealing the reduced binding stability.

The MD simulation results indicated that **SB2** exhibited improved binding behaviour compared to SUL in terms of binding stability, interaction persistence, and dynamic control within the DHPS active site. **SB2** maintained a consistent binding orientation, reduced protein flexibility in key functional regions, supported by electrostatic, hydrogen-bonding, and hydrophobic interactions. On the other hand, SUL exhibited more ligand mobility and less persistent interaction within the pocket. These findings suggest that **SB2** exhibits more stable binding behaviour toward DHPS under dynamic conditions.

4.3.2.1.3. MM-GBSA binding energy analysis. The MM-GBSA analysis was performed to estimate the binding free energy of the ligand within the DHPS active site. The MM-GBSA energy decomposition plots (Fig. 13a and b) suggested that **SB2** exhibited more favourable binding free energy than SUL. The binding was mainly driven by van der Waals (ΔG_{vdW})

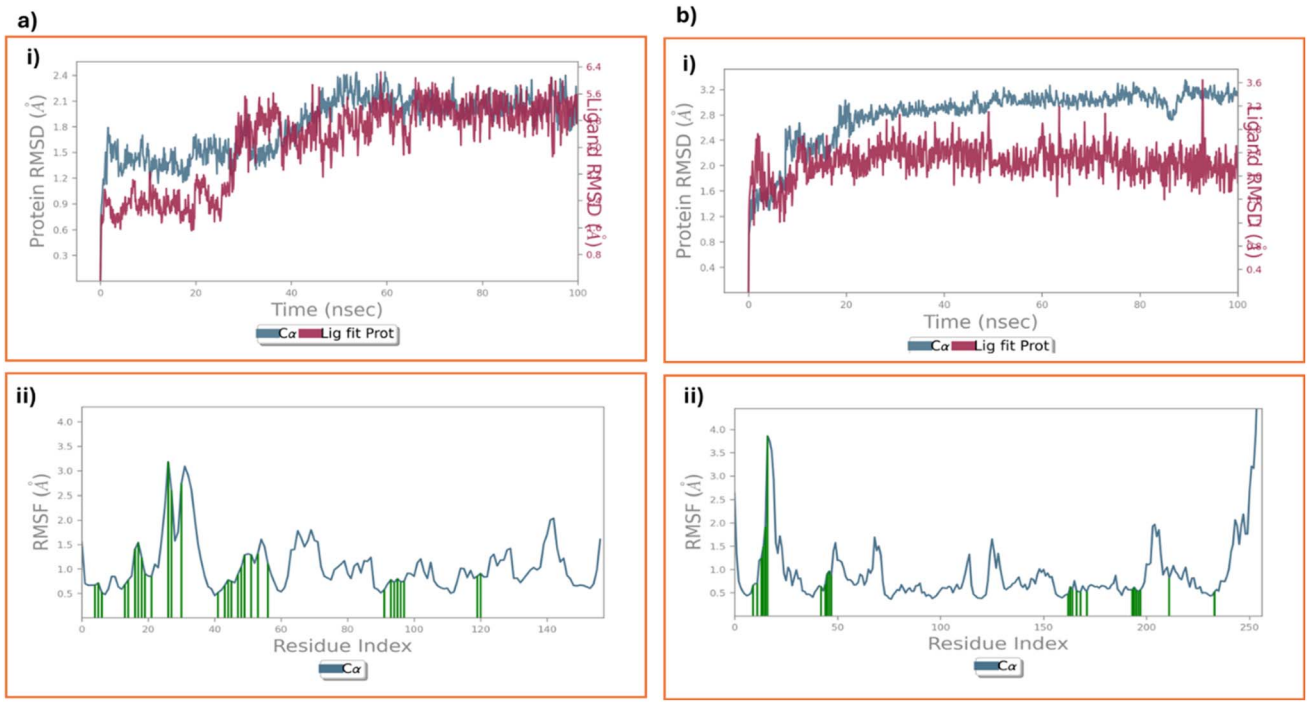

Fig. 11 The RMSD profiles for (ai) **SB2**-DHPS and (bi) SUL-DHPS provide useful information about the protein-ligand complexes' dynamic stability and conformational behavior during the 100 ns molecular dynamics simulations. (aii) **SB2** and (bii) SUL offer RMSF profiles for C_α atoms. The light blue and orange parts depict α-helices and β-sheets, respectively, while green bars represent residues that interact with ligands.

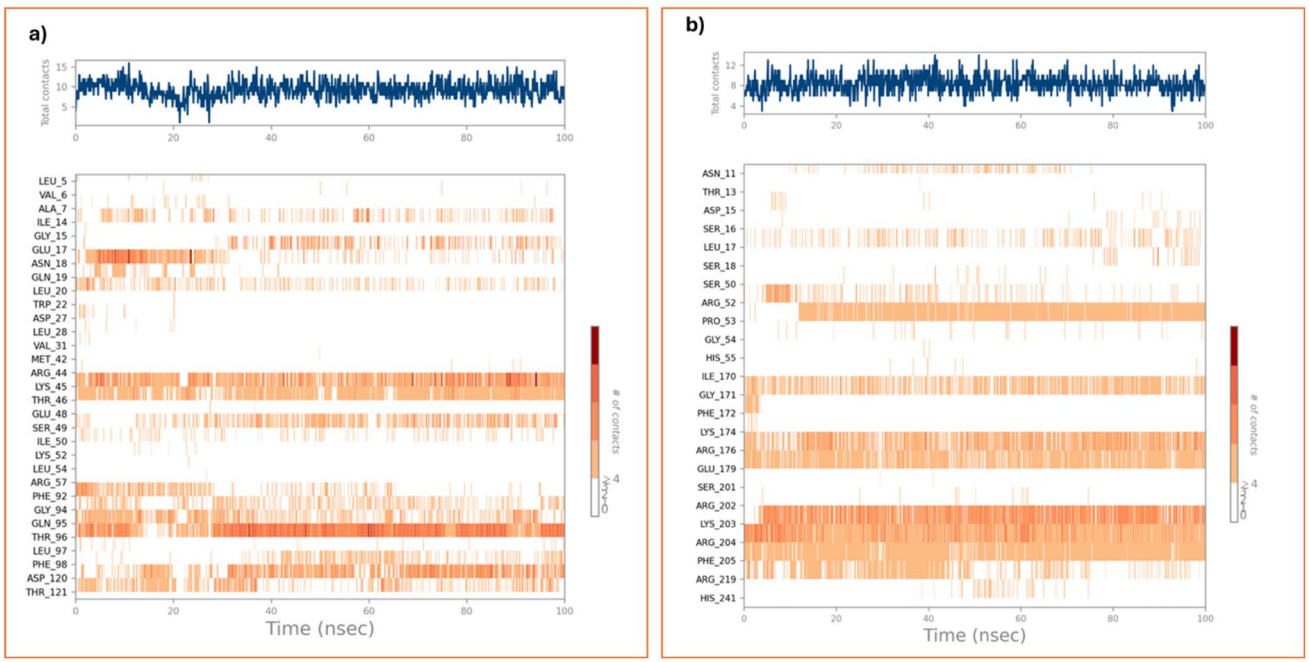

Fig. 12 Protein–ligand interaction timeline analysis of (a) **SB2**-DHPS and (b) SUL-DHPS complexes over 100 ns MD simulation. The upper panel represents total protein–ligand contacts over time, indicating interaction stability, while the lower heat map shows residue-wise interaction persistence, with darker orange shades highlighting key active-site residues.

interactions with contributions from lipophilic (ΔG_{Lipo}) and electrostatic (Coulomb) terms. The coulombic interactions showed more variation during the simulation, while hydrogen bonding and covalent contributions were small in both systems. In contrast, SUL had similar but slightly less favourable van der Waals contributions, with more variable electrostatics. The

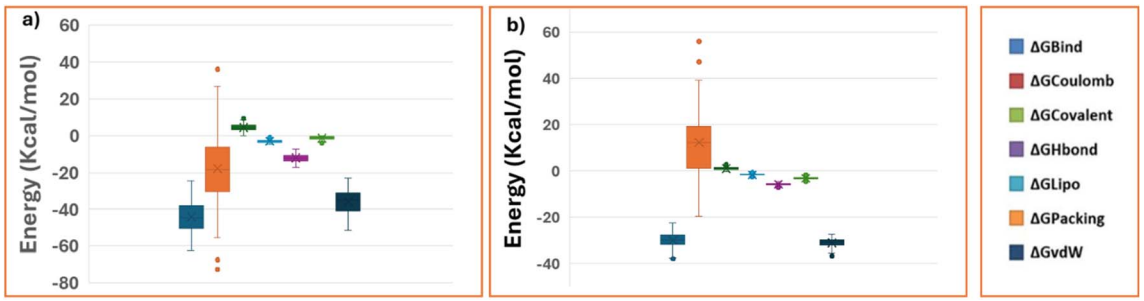

Fig. 13 Binding free energy components for docking complexes with DHPS protein, determined using MM-GBSA analysis for (a) **SB2** and (b) SUL.

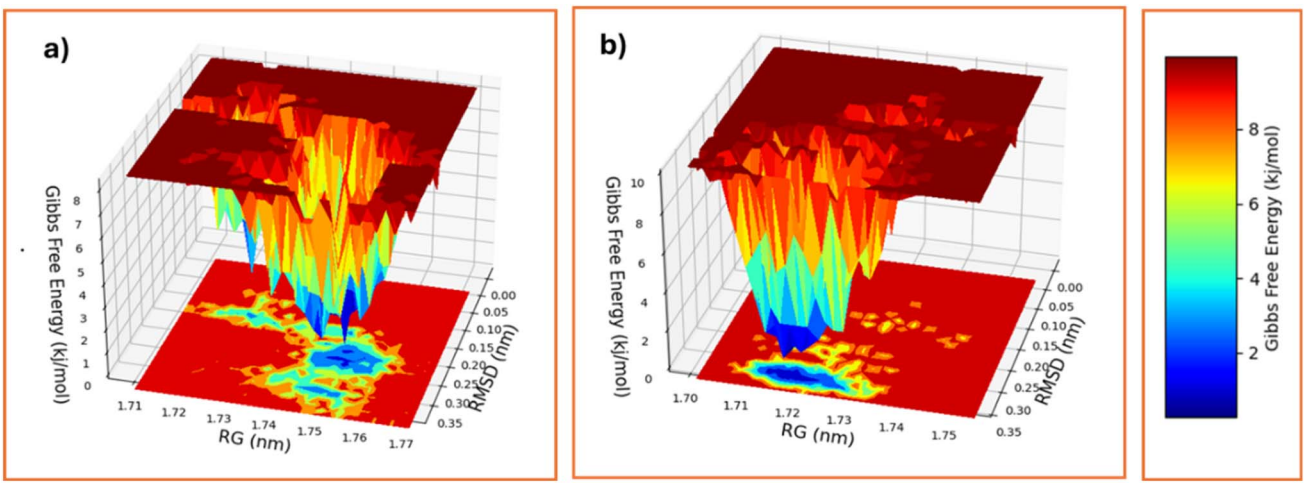

Fig. 14 FEL study of ligand-DHPS complexes based on molecular dynamics simulations. The graphs depict the Gibbs free energy (in kJ mol^{-1}) as a function of radius of gyration (R_g) and root-mean-square deviation (RMSD) for (a) **SB2**, and (b) SUL. The deep blue patches represent low-energy, highly stable conformational states.

packing energy ($\Delta G_{Packing}$), showed larger variations, thus indicating a higher variability in the interaction energetics. These findings indicate that **SB2** has more favourable binding energetics in the DHPS active site than SUL.

4.3.2.1.4. Free energy landscape (FEL) analysis. The MD trajectory was used for the FEL representation in terms of the conformational space of the **SB2**-DHPS and SUL-DHPS complexes (Fig. 14a and b). The **SB2**-DHPS complex exhibited a well-defined and deep energy minima and narrow low-energy basin, indicating a preferred conformational state with limited structural variation. On the other hand, the SUL-DHPS complex revealed a broad and more dispersed energy landscape with multiple shallow minima. This indicates that the SUL-DHPS complex has more conformations during simulation. In short, **SB2** provides more confined conformational state compared to SUL within the DHPS active site.

4.3.2.1.5. Principal component analysis (PCA). PCA was performed on the Cartesian coordinates derived from molecular dynamics trajectories to evaluate further insight into the large-scale conformational motions of the SUL-DHPS and **SB2**-DHPS complexes (Fig. 15a and b). Two-dimensional projections along the principal components (PC1–PC2, PC2–PC3, PC8–PC9, and PC9–PC10) revealed distinct conformational sampling behaviour for two systems.

The SUL-DHPS complex occupied a broader conformational space, with multiple overlapping clusters observed in the PC1–PC2 and PC2–PC3 projections, indicating higher conformational flexibility and frequent transitions between structural states. This behavior suggests that the protein explores a wider range of conformations in the presence of SUL. In contrast, the **SB2**-DHPS complex showed more compact and well-defined clustering across all the PCA projections, especially between PC1 and PC2 and between PC2 and PC3. The densely clustered trajectories indicate constrained large-scale motions and reduced conformational variability during the simulations. Overall, these results suggest that **SB2** promotes a more conformational behaviour of DHPS compared to SUL.[41]

4.3.2.1.6. Dynamic cross-correlation matrix (DCCM). DCCM analysis was performed to examine correlated and anti-correlated residue motions in the **SB2**-DHPS and SUL-DHPS (Fig. 16a and b). In the correlation maps, positive correlations (cyan) indicate residues moving in the same direction, whereas negative correlations (magenta) represent residues moving in opposite directions. The **SB2**-DHPS complex exhibited stronger

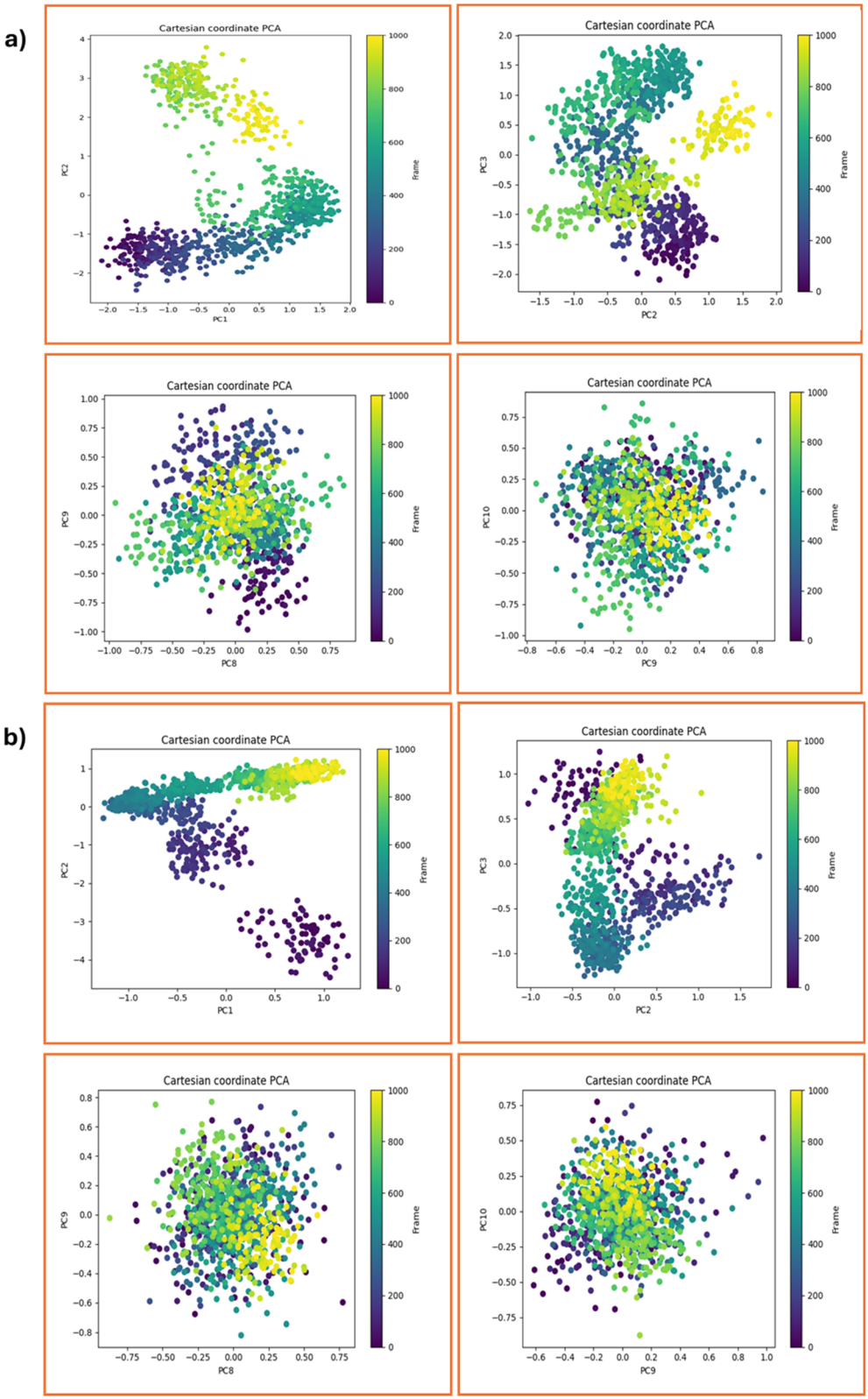

Fig. 15 A PCA study of the molecular dynamics trajectories for (a) **SB2** and (b) SUL revealed critical insights into their conformational dynamics and structural stability upon interaction with the DHPS target.

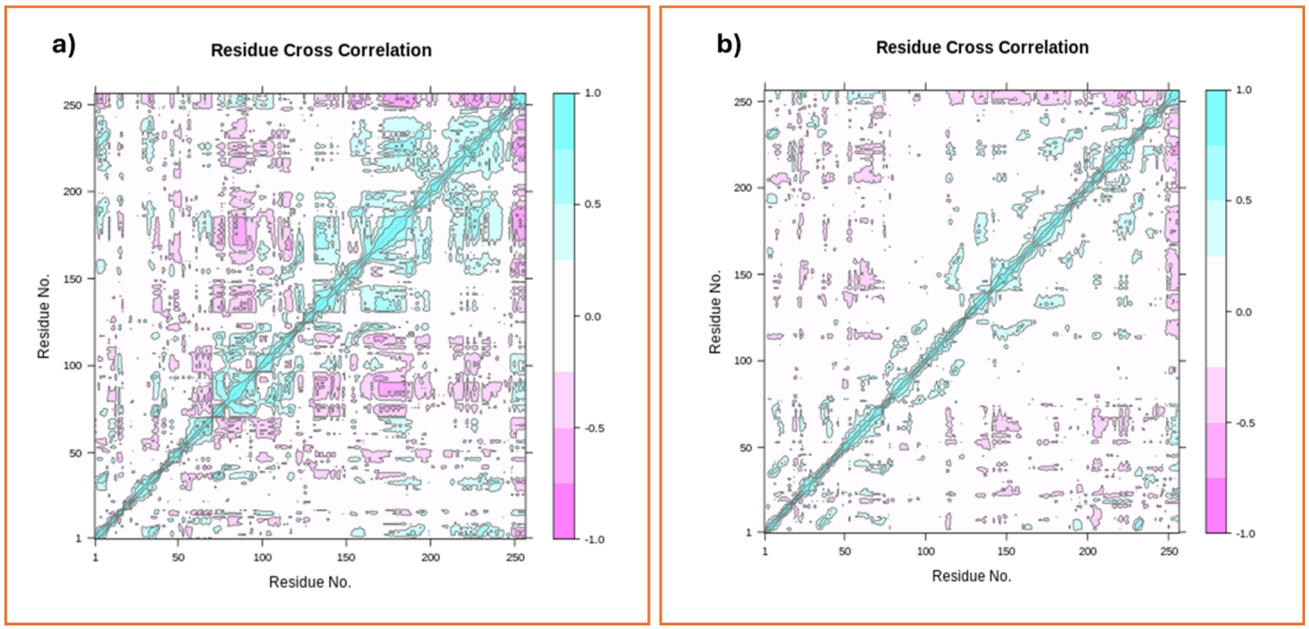

Fig. 16 Dynamic cross-correlation matrix (DCCM) plots of DHPS residue variations during binding to (a) **SB2** and (b) SUL. Cyan patches represent positively correlated movements, whereas magenta regions suggest anti-correlated motions.

and more structured correlated motions, especially diagonally and in a few off-diagonal locations. These extended regions of positive correlation indicate coordinated residue movements across the DHPS structure, suggesting efficient inter-domain communication. Moreover, the reduced intensity and limited distribution of anti-correlated motions indicate dampened internal oscillations, suggesting that **SB2** binding stabilized DHPS dynamics and promoted synchronized structural motions. However, the pattern of cross-correlations associated with the SUL-DHPS was weaker and more fragmented. In the cross-correlation map, there were fewer positively correlated motions and more scattered anti-correlated motions. This disrupted pattern suggested an increased structural flexibility and

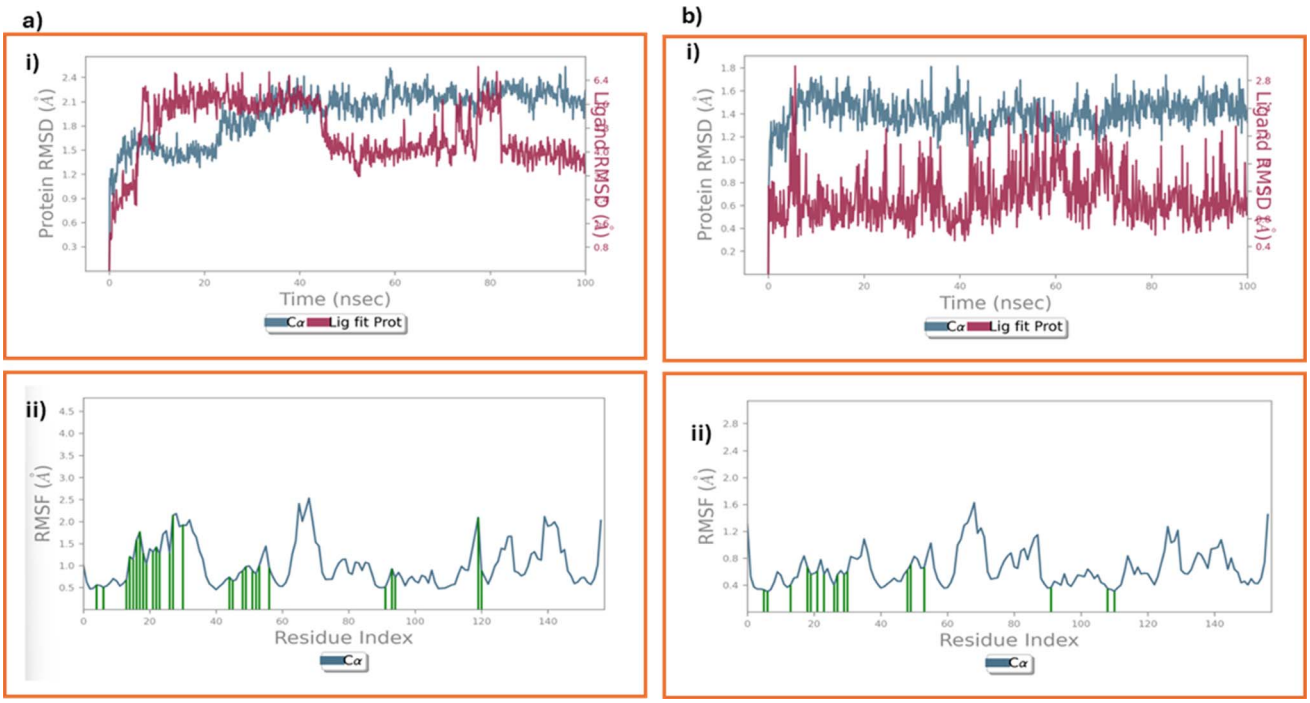

Fig. 17 The RMSD profiles for (ai) **SB5** and (bi) TMP give useful information about the ligand-DHFR complexes' dynamic stability and conformational behavior during the 100 ns molecular dynamics simulations. (aii) **SB5**, and (bii) TMP offer RMSF profiles for C_α atoms.

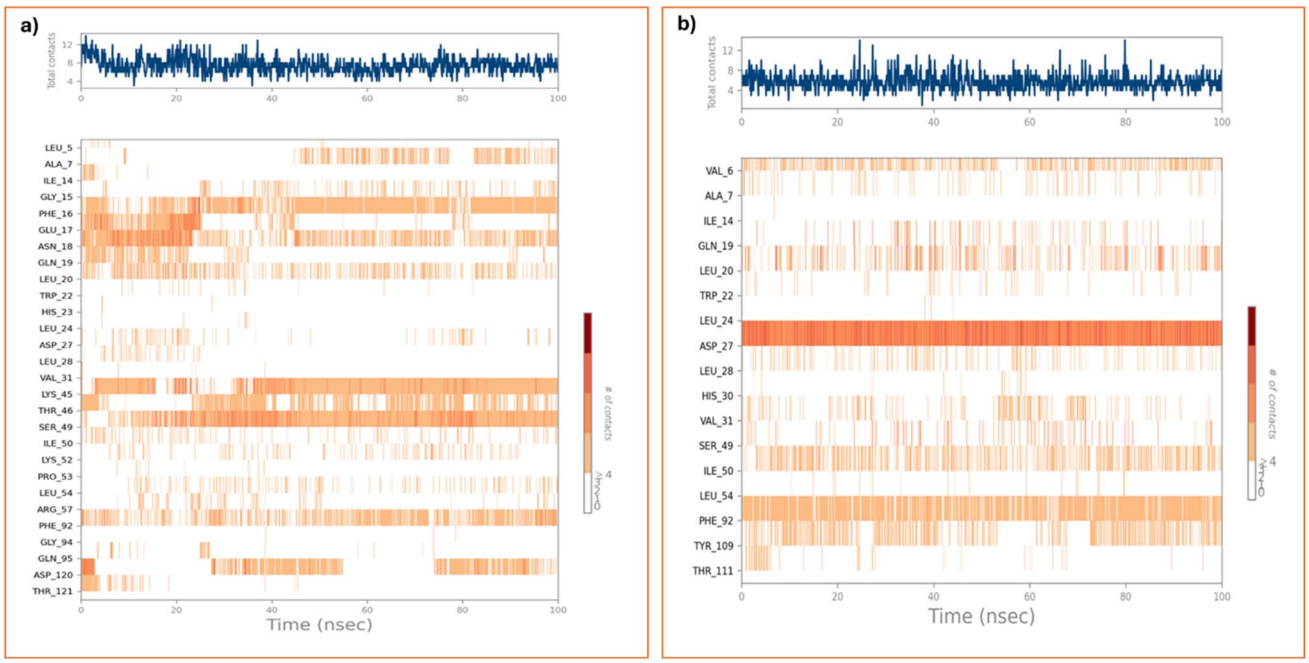

Fig. 18 Protein–ligand interaction timeline analysis of (a) SB5-DHFR and (b) TMP-DHFR complexes over 100 ns MD simulation. The upper panel represents total protein–ligand contacts over time, indicating interaction stability, while the lower heat map shows residue-wise interaction persistence, with darker orange shades highlighting key active-site residues.

diminished cooperative residue motion, indicative of less dynamically stable binding interactions.

Overall, the combined MD analysis indicate that **SB2** exhibits more consistent binding behaviour, favourable energetics, and more confined conformational dynamics within the active site of DHPS compared to SUL.

4.3.2.2 Molecular dynamics and free energy analysis of DHFR complexes

4.3.2.2.1. RMSD and RMSF analysis. Further RMSD profiling over 100 ns revealed that the **SB5**-DHFR complex reached equilibrium within the first 10 ns and remained consistent through the simulation (Fig. 17a). The DHFR backbone RMSD fluctuated within 1.9–2.3 Å, while the ligand RMSD remained within 1.2–1.6 Å, indicating consistent binding of **SB5** within the active site. Minor fluctuations in ligand RMSD were observed and can be attributed to conformational adjustment during the simulation. In contrast, the TMP-DHFR complex exhibited lower protein backbone deviation (1.3–1.6 Å), and lower ligand RMSD (0.4–0.9 Å), indicating a more rigid binding and very minor positional drift. Which is consistent with the docking score (Fig. 17b).

RMSF analysis further provided insight about the flexibility at the residue level. While the **SB5**-DHFR complex exhibited moderate flexibility, with RMSF values primarily in loop and terminal regions, while residues near the active site exhibited relatively controlled flexibility. In comparison the TMP-DHFR complex displayed overall lower RMSF values, indicating reduced residue-level motion and a more rigid conformational profile. Overall **SB5** displayed consistent binding behavior with moderate flexibility, whereas TMP exhibited more constrained binding mode withing the active site of DHFR.

4.3.2.2.2. Protein–ligand interaction analysis. The **SB5**-DHFR complex exhibited a moderate and sustained number of

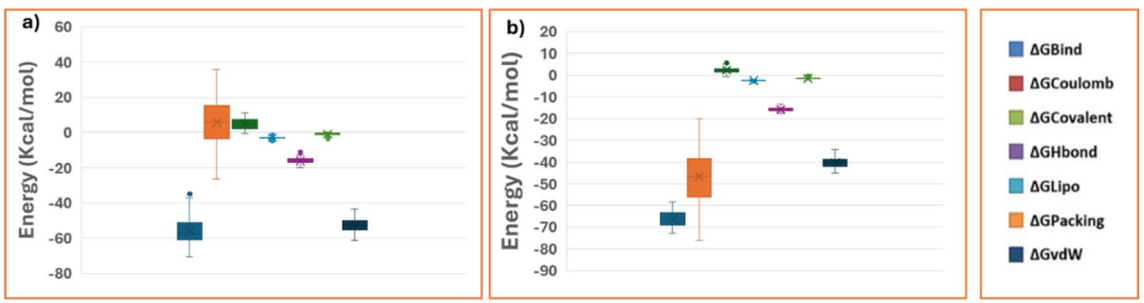

Fig. 19 Binding free energy components for docking complexes with DHFR protein, determined using MM-GBSA analysis for (a) **SB5**, and (b) TMP.

contacts throughout the simulation, with interactions distributed across multiple residues (Fig. 18a and b). The interaction heatmap indicates that residues such as GLU17, ASN18, LYS45, THR46, and PHE92 contributed intermittently, reflecting dynamic and distributed ligand engagement within the active site.[42] In contrast, the TMP-DHFR complex displayed a comparatively consistent interaction profile, with fewer but more persistent contacts localized around key residues. The heatmap revealed continuous interaction patterns with residues such as ASP27 and neighbouring residues, indicating a more focused interaction region.[43] Overall, **SB5** demonstrated a distributed interaction pattern with moderate persistence, whereas TMP exhibited a more localized and consistent interaction profile within the DHFR binding pocket.

4.3.2.2.3. MM-GBSA binding energy analysis. The MM-GBSA analysis demonstrated that both **SB5** and TMP exhibited favourable binding free energies within the DHFR (Fig. 19a and b). Total binding free energy (ΔG_{bind}) was influenced by electrostatic interactions, and van der Waals forces, with additional contributions from lipophilic interactions, and packing energies. TMP showed a comparatively more binding free energy, associated with consistent van der Waals and electrostatic contributions. In contrast, **SB5** demonstrated a slightly less favourable energy profile, with higher variation across certain energetic components, suggesting increased conformational adaptability during the simulation.[44] These results indicate that TMP exhibits more favourable binding energetics, while **SB5** maintains comparable interaction contributions, supporting its potential as a viable lead scaffold for further optimization toward the DHFR.

4.3.2.2.4. Free energy landscape (FEL) analysis. In comparison with the TMP, the **SB5**-DHFR complex exhibited a broader and more dispersed free energy landscape (Fig. 20a and b). **SB5** occupied a broader low-energy basin with multiple minima, indicating increased conformational flexibility during the simulation. This suggests that **SB5** explores a range of conformational; states within the DHFR active site. In contrast, TMP showed deep and well-defined global minima, indicating strong ligand–protein interaction and a narrow energy basin associated with reduced confirmational variability. This indicates that TMP predominately occupied a limited conformations during the simulation. Overall, these observations suggest that **SB5** exhibits greater conformational adaptability, whereas TMP exhibits a more confined conformational profile. The broader conformational sampling observed for **SB5** may provide a scope for structural optimization to enhance the stability and positioning as a lead compound for future modification.

4.3.2.2.5. Principal component analysis (PCA). The PCA projection of the TMP-DHFR complex revealed a highly compact and well-clustered distribution across the principal components (PC1–PC2, PC2–PC3, PC8–PC9, and PC9–PC10) (Fig. 21a), indicating that the complex occupies a relatively confined conformational space. The limited dispersion of trajectory frames reflects restricted large-scale motions during the simulation. On the other hand, the **SB5**-DHFR complex exhibited a broader and more dispersed conformational distribution (Fig. 21b), with multiple clusters along the principal axes. This suggests increased conformational flexibility and transition between conformational states. Overall, these results indicate that TMP is associated with a more confined conformational profile, whereas **SB5** exhibits greater conformational variability within the DHFR active site.

4.3.2.2.6. Dynamic cross-correlation matrix (DCCM). In the DCCM analysis, the **SB5**-DHFR complex demonstrated a combination of correlated and anti-correlated motions throughout the protein matrix (Fig. 22a), with several off-diagonal regions showing negative correlations. This indicates enhanced conformational flexibility and long-range dynamic interaction with distant residues. The TMP-DHFR complex showed a stronger and more consistent pattern of positive

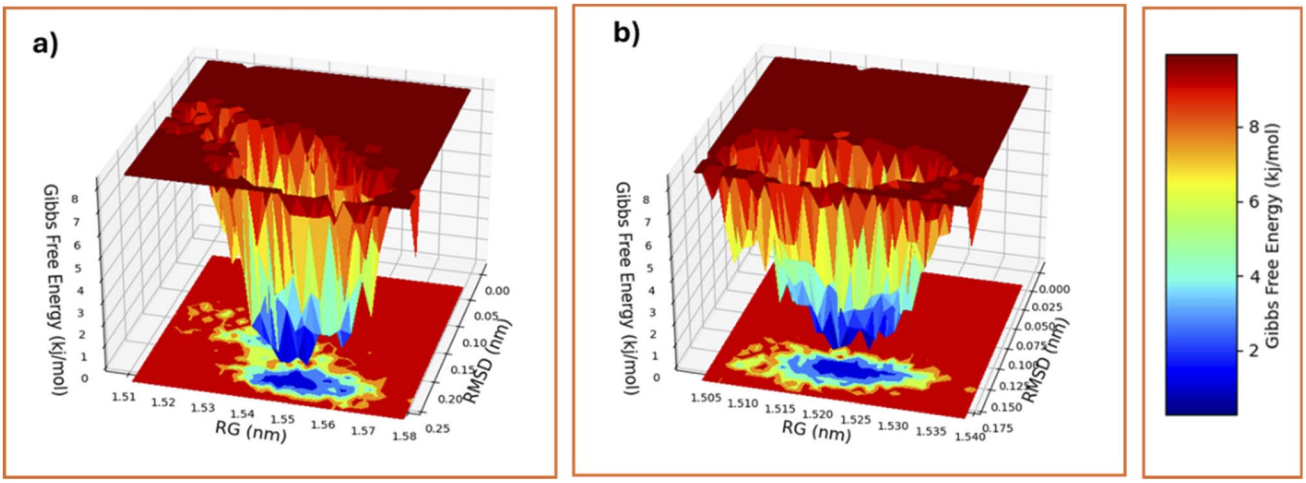

Fig. 20 FEL study of ligand-DHFR complexes based on molecular dynamics simulations. The graphs depict the Gibbs free energy (in kJ mol^{-1}) as a function of radius of gyration (R_g) and root-mean-square deviation (RMSD) for (a) **SB5**, and (b) TMP. The deep blue patches represent low-energy, highly stable conformational states.

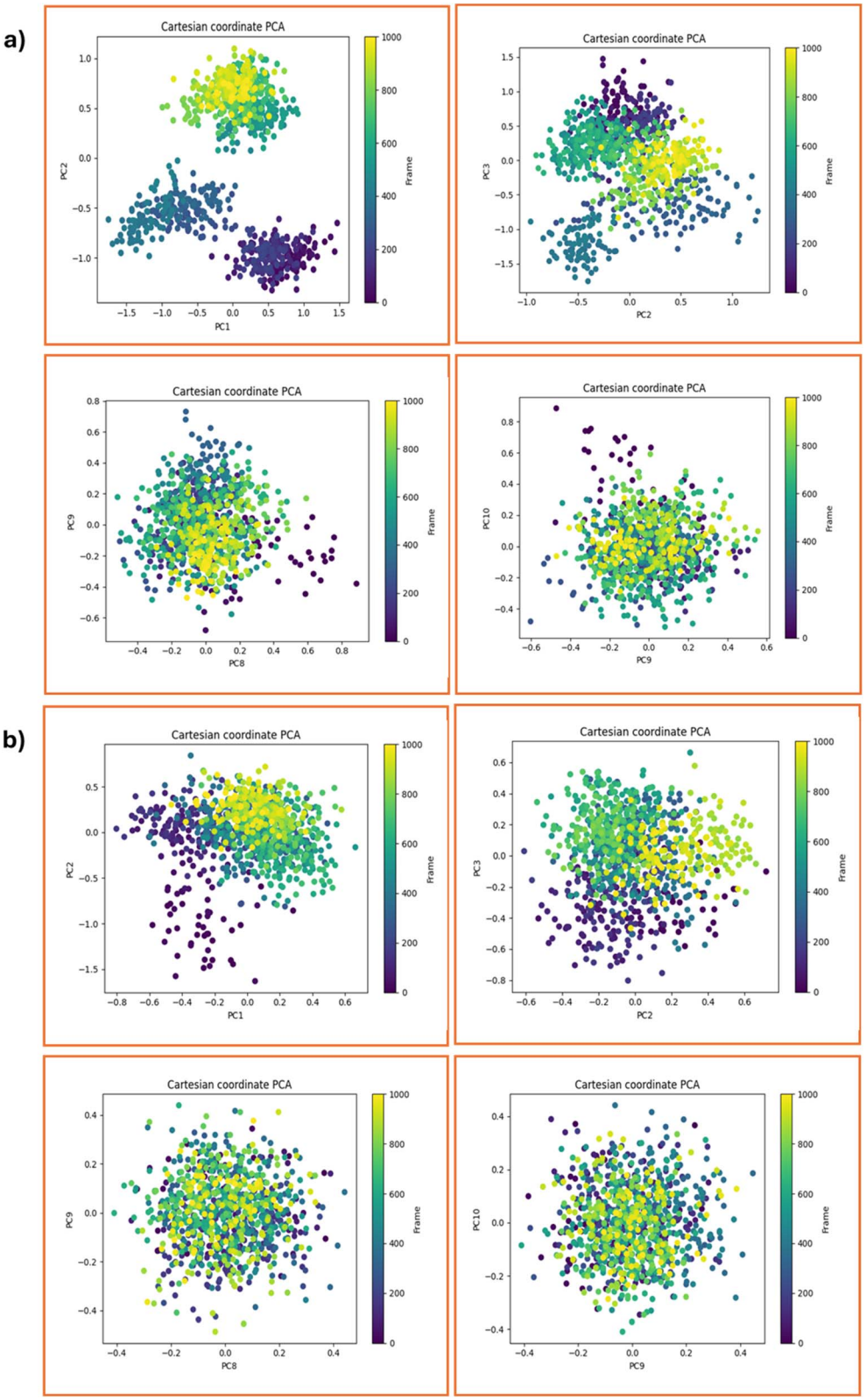

Fig. 21 A PCA study of the molecular dynamics trajectories for (a) **SB5**, and (b) TMP reveals critical insights into their conformational dynamics and structural stability upon interaction with the DHFR target.

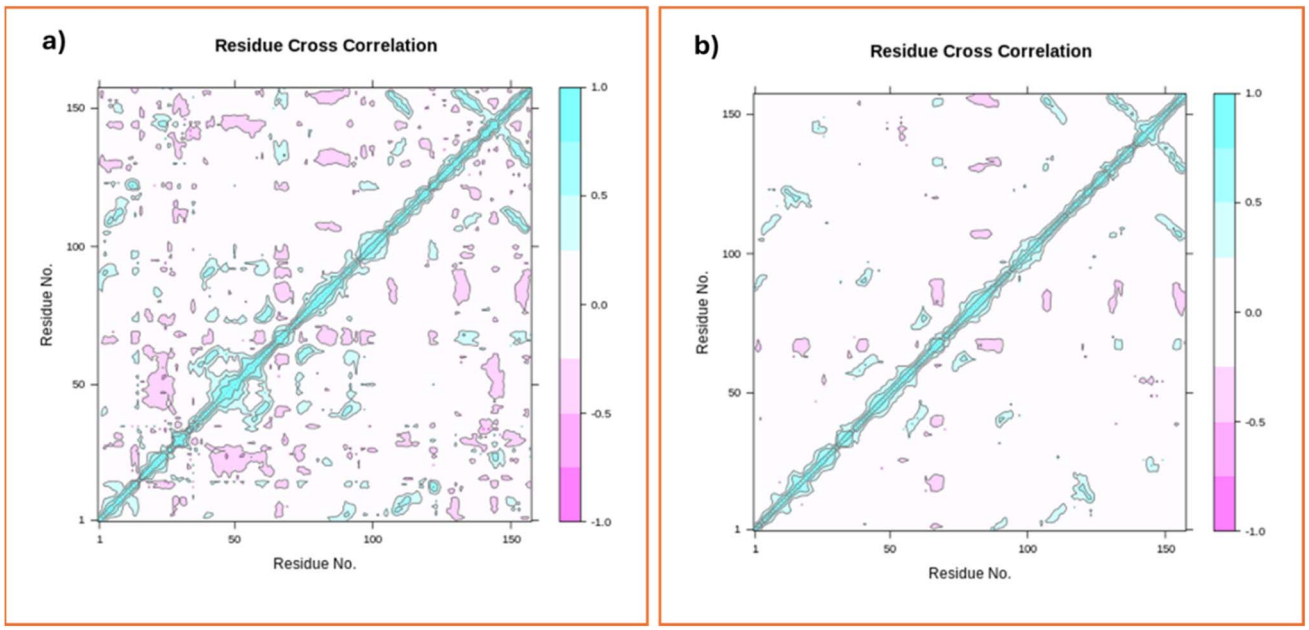

Fig. 22 Dynamic cross-correlation matrix (DCCM) plots of DHFR residue variations during binding to (a) **SB5**, and (b) TMP. Cyan patches represent positively correlated movements, whereas magenta regions suggest anti-correlated motions.

correlations along the diagonal, with fewer and less pronounced anti-correlated regions (Fig. 22b). This indicates more coordinated residue motions across the protein. TMP stabilizes the DHFR framework and leads to synchronized residue motions.[45] Overall, these observations indicate that **SB5** is associated with more variable dynamic behaviour, whereas TMP shows more coordinated residue motion within the DHFR.

In summary, MD analyses revealed that **SB5** exhibits greater conformational variability and adaptive binding behaviour withing the DHFR active site, whereas TMP associated with a more confined and coordinated conformational profile. Despite this difference, **SB5** maintains consistent interaction patterns and favourable binding energetics, supporting its potential as a promising scaffold for further optimalization.

Importantly, the computational findings are consistent with the observed experimental trends. **SB2** showed a preferential binding behaviour and confined conformational dynamics towards DHPS, in line with its enhanced inhibition compared to Sul, supporting its potential as a promising DHPS-directed scaffold. **SB5** exhibited comparable DHFR inhibitory activity relative to TMP, consistent with the computational findings. While TMP showed a more constrained binding profile, **SB5** demonstrated adaptable conformational behavior with sustained interaction patterns. These observations collectively support the relevance of the computational analyses in rationalizing the experimentally observed activity and highlight **SB2** and **SB5** as promising scaffolds for further optimization.

4.3.3 *In Silico* toxicity evaluation. *In silico* ADMET parameters were obtained from QikProp, toxicity predictions from Protox-II (3.0), and gastrointestinal absorption and blood–brain barrier permeability were assessed using the BOILED-Egg model implemented in SwissADME (Fig. 23). Notably, **SB4** and **SB7** had better oral absorption compared to **SB6**, whose absorption was relatively poor, implying that further optimization of structure will help improve bioavailability. On the other hand, the SUL had moderate oral absorption similar to compounds. Further, **SB1–SB7** had low permeability into the central nervous system (log BB of −2.04 to −1.11) showing that they would not cross the blood–brain barrier hence low likelihood of central nervous system toxicity. In addition, **SB1–SB7** had moderate lipophilicity (QPlogPo/w from 2.39 to 4.64) hence their membrane permeation capability and ease of absorption.[46] On the other hand, SUL had low lipophilicity which implies poor permeation capability. Furthermore, compounds **SB1–SB7** showed good compliance with Lipinski's rule of five, with only **SB5** and **SB6** presenting a single violation, indicating favourable drug-likeness properties (Table 7). The polar surface area (PSA) values were relatively higher for **SB2** and **SB6**, which may explain their comparatively lower absorption profiles. The predicted protein binding (QPlogKhsa) values indicated moderate interaction with serum albumin for compounds **SB1–SB7**, with **SB5** showing relatively stronger binding affinity, while SUL exhibited weaker binding.

Regarding toxicity prediction, compounds **SB1–SB7** demonstrated acceptable safety profiles with LD_{50} values ranging from 500 to 1000 mg kg^{-1}, while SUL showed a higher safety margin. Notably, none of the compounds exhibited mutagenicity except **SB6**, which was predicted to be active and may require further structural modification. Additionally, all compounds were predicted to be non-immunotoxic, indicating a favourable safety profile.

Importantly, the *in silico* toxicity predictions for **SB2** are consistent with the experimental findings. **SB2** exhibited high cell viability in the MTT assay and did not induce DNA damage

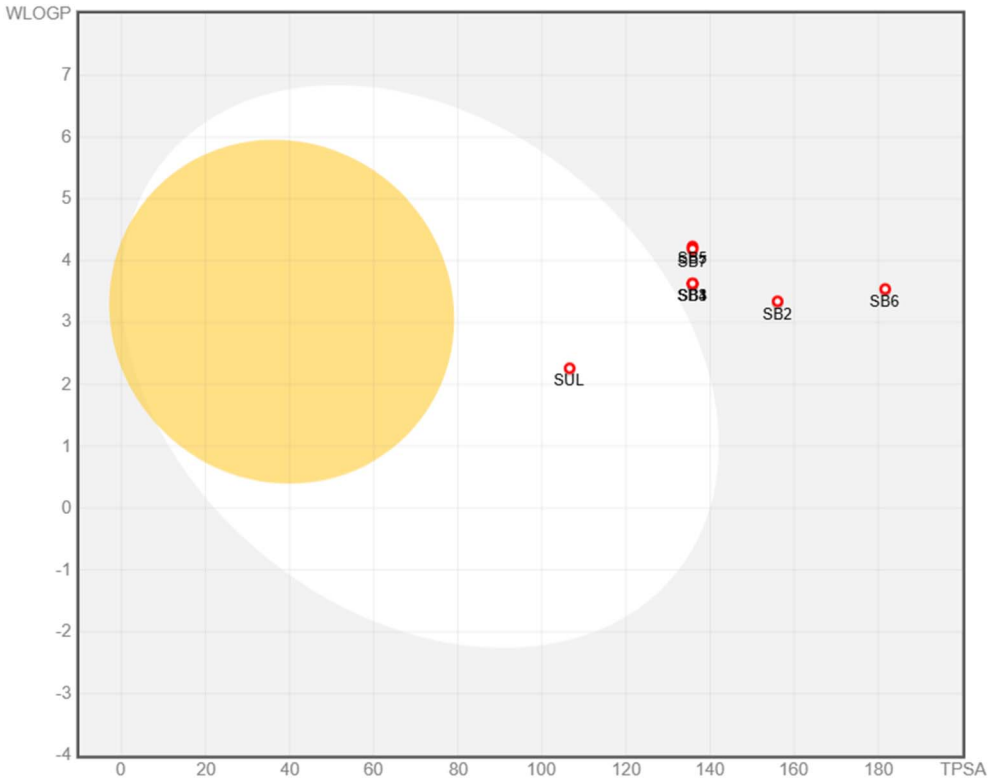

Fig. 23 The Boiled-egg diagram for the compounds **SB1–SB7**, along with SUL as a standard drug.

Table 7 *In silico* ADMET (QikProp) and toxicity (Protox-3.0) profiles of compounds **SB1–SB7** compared with the SUL, highlighting drug-likeness, mutagenicity and immunotoxicity

Compound	SB1	SB2	SB3	SB4	SB5	SB6	SB7	SUL
QikProp ADMET								
QPlogPo/w	3.43	2.39	3.09	4.13	4.64	2.98	3.18	0.49
LogBB	−2.04	−1.55	−1.34	−1.63	−1.45	−1.72	−1.11	−1.38
Oral Abs (%)	73.62	66.86	76.31	83.25	72.48	55.29	78.26	70.06
PSA (Å^2)	134.38	151.67	130.2	127.47	129.71	167.6	130.14	103.37
QPlogKhsa	0.054	−0.235	−0.088	0.217	0.343	−0.102	−0.098	−0.605
Ro5	0	0	0	0	1	1	0	0
Protox-3.0 Toxicity								
LD_{50} (mg kg^{-1})	1000	1000	1000	500	500	500	1000	2300
Mutagenicity	Inactive	Inactive	Inactive	Inactive	Inactive	Active	Inactive	Inactive
Immunotoxicity	Inactive	Inactive	Inactive	Inactive	Inactive	Inactive	Inactive	Inactive

in the DNA nicking study, indicating a favourable safety profile. In line with these observations, Protox-3.0 predicted a moderate LD_{50} value (1000 mg kg^{-1}) along with an inactive immunotoxicity profile which aligns with its experimentally observed biocompatibility. Furthermore, the chemical stability of **SB2** was assessed by HPLC over 72 h under physiological conditions. No significant changes in retention time or peak profile were observed, indicating the absence of detectable degradation. This confirms that the biological and computational outcomes are attributable to the intact compound and not influenced by degradation products. These findings suggest that **SB2** maintains biological activity without inducing significant cytotoxic or genotoxic effects under the studied conditions. Collectively, the results indicate a favourable safety profile for **SB2**, although further *in vitro* and *in vivo* studies are required to confirm these observations.

5. Conclusion

In the present study, seven designed molecules of PABA Analogues were successfully synthesized by using the microwave-assisted green chemistry approach with the efficient yield (72–92%). All compounds show potent and comparable antimicrobial activity compared to standard drugs. **SB2**

demonstrated superior activity (2 μg mL^{-1}) compared to the SUL–TMP combination (8 μg mL^{-1}) against MRSA and also showed higher activity (8 μg mL^{-1}) than amoxicillin (16 μg mL^{-1}) against XDR *E. coli.* In comparison with the IC_{50} results by folate inhibition assay, **SB2** (IC_{50}: 0.098 ± 0.005 μg mL^{-1}) outperformed SUL (IC_{50}: 0.104 ± 0.005 μg mL^{-1}), while **SB5** exhibited comparable results with the TMP for DHFR inhibition. These results were supported by the molecular dynamics, PCA, FEL, and DCCM analysis. **SB2** also showed potent antioxidant activity and DNA nicking ability. The cytotoxicity assay confirmed that **SB2** is nontoxic and biocompatible even at higher concentrations. In addition, *in silico* ADMET analysis indicated favourable pharmacokinetic properties with low CNS penetration, supporting the reliability of the biological findings. Overall, this integrated experimental and computational evaluation suggests **SB2** as a promising dual DHPS/DHFR inhibitor and highlights **SB5** as a lead scaffold with strong potential for further development against antimicrobial resistance and folate pathway targets. Furthermore, extensive toxicological studies including *in vivo* acute toxicity studies will be undertaken as immediate future work to further validate the safety profile of these compounds.

Author contributions

Bhargav Devliya is responsible for the conception and design of the study, synthesis of the compounds, molecular docking, and data interpretation, as well as drafting the manuscript. Ahmed Al-Kubeisi and Botros Y. Beshay performed the enzyme binding assay and assisted with the interpretation of enzymatic inhibition results. Nandan Dixit and Saumya Patel performed the computational study and molecular modelling analysis. Milan Thakar and Gaurang Sindhav performed antioxidant and cytotoxicity assays and assisted with the interpretation of results. Drashti Patel, Milan Dabhi, Kiransinh Rajput, and Dweipayan Goswami performed microbiology, including antimicrobial activity evaluation and result interpretation. Bimalkumar Patel assisted with compound characterization, spectral analysis, and validation of results. Jaykumar Nagapara and Shreya Chauhan assisted with the study, manuscript compilation, and manuscript drafting. Hitesh D. Patel supervised the study, assisted with the conception of the study.

Conflicts of interest

The authors declare that there are no conflicts of interest.

Data availability

All the required data and information are included in the manuscript and supplementary information (SI) file. Supplementary information is available. See DOI: https://doi.org/10.1039/d6ra01925k.

Acknowledgements

The authors gratefully acknowledge the Department of Chemistry, Gujarat University, for providing access to e-resources and laboratory facilities. The Department of Microbiology, Gujarat University, is sincerely acknowledged for carrying out antimicrobial evolution. The authors are also thankful to the Department of Zoology, Gujarat University, for the antioxidant activity, DNA nicking assay, and cytotoxicity evaluation. Authors acknowledge the Department of Bioinformatics, Gujarat University, for computational studies. The authors further express their sincere thanks to the College of Pharmacy, University of Al Maarif, Iraq, and the Pharmaceutical Sciences Department, College of Pharmacy, Arab Academy for Science, Technology, and Maritime Transport, Alexandria, Egypt, for their support in the enzyme binding assay.

References

1 B. Devliya, B. Patel, S. J. Chauhan and H. D. Patel, A Comprehensive Review of Nanomaterials as Potential Weapons against Multidrug-Resistant Staphylococcus Aureus, *Pharm. Nanotechnol.*, 2025, **13**(5), 865–884, DOI: 10.2174/0122117385314186240522100239.

2 S. Sharma, A. Chauhan, A. Ranjan, D. M. Mathkor, S. Haque, S. Ramniwas, H. S. Tuli, T. Jindal and V. Yadav, Emerging Challenges in Antimicrobial Resistance: Implications for Pathogenic Microorganisms, Novel Antibiotics, and Their Impact on Sustainability, *Front. Microbiol.*, 2024, **15**, 1403168, DOI: 10.3389/fmicb.2024.1403168.

3 H. A. Sheerah, A. R. Algwizani, R. Q. Alghamdi, E. L. Almohammadi, A. M. Al-Qunaibe, H. M. Dada, H. S. Algarni, S. M. Tunkar, A. M. Altamimi, Y. S. Almuzaini and D. Selbie, Strengthening Global Health Security through Antimicrobial Resistance Control: Insights from Saudi Arabia, *J. Infect. Public Health*, 2025, **18**(7), 102788, DOI: 10.1016/j.jiph.2025.102788.

4 G. Muteeb, M. T. Rehman, M. Shahwan and M. Aatif, Origin of Antibiotics and Antibiotic Resistance, and Their Impacts on Drug Development: A Narrative Review, *Pharmaceuticals*, 2023, **16**(11), 1615, DOI: 10.3390/ph16111615.

5 Q. Xu, X. Hu and Y. Wang, Alternatives to Conventional Antibiotic Therapy: Potential Therapeutic Strategies of Combating Antimicrobial-Resistance and Biofilm-Related Infections, *Mol. Biotechnol.*, 2021, **63**(12), 1103–1124, DOI: 10.1007/s12033-021-00371-2.

6 C. Bourne, Utility of the Biosynthetic Folate Pathway for Targets in Antimicrobial Discovery, *Antibiotics*, 2014, **3**(1), 1–28, DOI: 10.3390/antibiotics3010001.

7 Á. Kerek, B. Török, Á. Szabó, L. Laczkó, G. Kardos, K. Bányai, E. Kaszab, K. Bali and Á. Jerzsele, Resistance Evolution under Potentiated Sulphonamide Pressure in Escherichia Coli, *Front. Vet. Sci.*, 2025, **12**, 1697872, DOI: 10.3389/fvets.2025.1697872.

8 A. Ovung and J. Bhattacharyya, Sulfonamide Drugs: Structure, Antibacterial Property, Toxicity, and Biophysical

Interactions, *Biophys. Rev.*, 2021, **13**(2), 259–272, DOI: 10.1007/s12551-021-00795-9.
9 G. D. Wright, Mechanisms of Resistance to Antibiotics, *Curr. Opin. Chem. Biol.*, 2003, **7**(5), 563–569, DOI: 10.1016/j.cbpa.2003.08.004.
10 D. I. Hammoudeh, Y. Zhao, S. W. White and R. E. Lee, Replacing Sulfa Drugs with Novel Dhps Inhibitors, *Future Med. Chem.*, 2013, **5**(11), 1331–1340, DOI: 10.4155/fmc.13.97.
11 P. A. Asyraf, I. F. Kusnadi, J. Stefanus, M. A. Khairinisa and R. Abdulah, Clinical Manifestations and Genetic Influences in Sulfonamide-Induced Hypersensitivity, *Drug Healthc. Patient Saf.*, 2022, **14**, 113–124, DOI: 10.2147/DHPS.S347522.
12 Y. Peng, Y. Yu, Z. Su, Y. Zhong, S. Vijayakumar, Y. Chen, Y. Mao, M. Xin and M. Li, Design, Synthesis, and Bioactivity Evaluation of PABA-Based Five- and Six-Membered Heterocyclic Schiff Base Quaternary Ammonium Chitosan Derivatives, *Carbohydr. Polym.*, 2025, **367**, 124015, DOI: 10.1016/j.carbpol.2025.124015.
13 K. Bredael, S. Geurs, D. Clarisse, K. De Bosscher and M. D'hooghe, Carboxylic Acid Bioisosteres in Medicinal Chemistry: Synthesis and Properties, *J. Chem.*, 2022, **2022**, 1–21, DOI: 10.1155/2022/2164558.
14 S. Thakare Suresh and A. K. Dhawas, Synthesis of Some New Imidazole-Thiols and Their Derivatives as Potent Antimicrobial Agents, *Indian J. Chem.*, 2014, **53**, 642–646.
15 K. Dhawas Amol, S. S. Thakare and N. R. Thakare, Synthesis and Characterization of Some New 1, 4, 5-Trisubstituted Imidazole-2- Thiols Derivatives, *J. Chem. Pharm. Res.*, 2012, **4**(1), 866–871.
16 *Clinical Microbiology Procedures Handbook*, ed.L. S. Garcia, H. D. Isenberg, Wiley, 2010, DOI: 10.1128/9781555817435.
17 F. Cockerill, *Methods for Dilution Antimicrobial Susceptibility Tests for Bacteria that Grow Aerobically : Approved Standard*; Clinical and Laboratory Standards Institute, 2015.
18 H. Ceri, M. E. Olson, D. W. Morck and D. G. Storey, Minimal Biofilm Eradication Concentration (MBEC) Assay: Susceptibility Testing for Biofilms, in *Biofilms, Infection, and Antimicrobial Therapy*, CRC Press, 2005, pp. 275–288, DOI: 10.1201/9781420028232-19.
19 S. D. Sarker, L. Nahar and Y. Kumarasamy, Microtitre Plate-Based Antibacterial Assay Incorporating Resazurin as an Indicator of Cell Growth, and Its Application in the in Vitro Antibacterial Screening of Phytochemicals, *Methods*, 2007, **42**(4), 321–324, DOI: 10.1016/j.ymeth.2007.01.006.
20 M. S. BLOIS, Antioxidant Determinations by the Use of a Stable Free Radical, *Nature*, 1958, **181**(4617), 1199–1200, DOI: 10.1038/1811199a0.
21 M. Thakar, P. Trivedi and G. Sindhav, Sustainable Biosynthesis of Silver Nanoparticles from Gmelina Arborea: Photocatalytic, in Vitro Biological Implications, and in Silico Analysis for Microbial Metalloproteins, *J. Mol. Liq.*, 2025, **422**, 126966, DOI: 10.1016/j.molliq.2025.126966.
22 H. I. Ansari, R. C. Dabhi, P. G. Trivedi, M. S. Thakar, J. J. Maru and G. M. Sindhav, Isolation and Characterization of Undescribed Flavonoid from Abrus Precatorius L. Based on HPTLC-DPPH Bioautography and Its Cytotoxicity Evaluation, *Future J. Pharmaceut. Sci.*, 2023, **9**(1), 119, DOI: 10.1186/s43094-023-00571-4.
23 M. Thakar, P. Trivedi and G. Sindhav, Sustainable Biosynthesis of Silver Nanoparticles from Gmelina Arborea: Photocatalytic, in Vitro Biological Implications, and in Silico Analysis for Microbial Metalloproteins, *J. Mol. Liq.*, 2025, **422**, 126966, DOI: 10.1016/j.molliq.2025.126966.
24 S. Gajewski, E. C. Griffith, Y. Wu and S. W. White, Staphylococcus Aureus Dihydropteroate Synthase (SaDHPS) F17L E208K Double Mutant Structure, *Worldwide Protein Data Bank*, 2018, DOI: 10.2210/pdb6clv/pdb.
25 S . M. Reeve, Wright, Staphylococcus aureus Dihydrofolate reductase in complex with NADPH and UCP1232, 2019, DOI: 10.2210/pdb6PBO/pdb.
26 G. Van Den Driessche and D. Fourches, Adverse Drug Reactions Triggered by the Common HLA-B*57:01 Variant: A Molecular Docking Study, *J. Cheminf.*, 2017, **9**(1), 13, DOI: 10.1186/s13321-017-0202-6.
27 R. A. Friesner, R. B. Murphy, M. P. Repasky, L. L. Frye, J. R. Greenwood, T. A. Halgren, P. C. Sanschagrin and D. T. Mainz, Extra Precision Glide: Docking and Scoring Incorporating a Model of Hydrophobic Enclosure for Protein−Ligand Complexes, *J. Med. Chem.*, 2006, **49**(21), 6177–6196, DOI: 10.1021/jm051256o.
28 R. A. Friesner, J. L. Banks, R. B. Murphy, T. A. Halgren, J. J. Klicic, D. T. Mainz, M. P. Repasky, E. H. Knoll, M. Shelley, J. K. Perry, D. E. Shaw, P. Francis and P. S. Shenkin, Glide: A New Approach for Rapid, Accurate Docking and Scoring. 1. Method and Assessment of Docking Accuracy, *J. Med. Chem.*, 2004, **47**(7), 1739–1749, DOI: 10.1021/jm0306430.
29 R. Dey, B. Patel, V. K. Vyas, N. Dixit, S. Patel and H. Bhatt, Structure-Guided Computational Design of Novel Polycyclic Aromatic Compounds as Telomerase Inhibitors for the Treatment of Cancer, *Netw. Model. Anal. Health Inform. Bioinform.*, 2025, **14**(1), 18, DOI: 10.1007/s13721-025-00511-7.
30 N. Dixit, H. Motwani, H. A. Solanki, R. M. Rawal and S. K. Patel, Integrative Bioinformatics Analysis for the Identification of Hub Genes and Virtual Screening of Phytochemicals to Inhibit AURKA in HepatoCellular Carcinoma, *Hum. Gene*, 2024, **41**, 201321, DOI: 10.1016/j.humgen.2024.201321.
31 S. Shaaban, S. S. Hawas, M. Sharaky, H. Ba-Ghazal, A. A. Elmaaty, K. B. Alomari, M. Alaasar, A. M. Elsharif, F. S. Alatawi, M. A. Mohamed, A. O. Al Khatib and A. A. Al-Karmalawy, Hybrid Benzylidene Thiazolidine-2,4-Diones as Potent Apoptosis-Inducing Anticancer Agents: Design-Driven Optimization, Cytotoxic Profiling, and Mechanistic Validation in Prostate Cancer, *RSC Adv.*, 2026, **16**(21), 19144–19157, DOI: 10.1039/D6RA01323F.
32 A. Porthouse, D. F. J. Brown, R. G. Smith and T. Rogers, GENTAMICIN RESISTANCE IN STAPHYLOCOCCUS AUREUS, *Lancet*, 1976, **307**(7949), 20–21, DOI: 10.1016/S0140-6736(76)92912-3.
33 O. Shemetov, M. Faustova, T. Perepelova, H. Balia, I. Pavlish and G. Loban', Forecasting the Development of

Antimicrobial Resistance of S. Aureus, *Front. Oral Health*, 2025, **5**, 1514070, DOI: 10.3389/froh.2024.1514070.

34 S. Asif, S. Muhammad Nur Farhan, Y. Nor Afnizan Mohd, Z. Noraziah Mohamad and R. Abdul Rahim Abdul, Differences in Antibiotic Resistance Profiles of Methicillin-Susceptible and –Resistant Staphylococcus Aureus Isolated from the Teaching Hospital in Kuala Lumpur, Malaysia, *J. Appl. Biol. Biotechnol.*, 2020, **9**(4), 98–103, DOI: 10.7324/JABB.2021.9413.

35 E. B. Kurutas, The Importance of Antioxidants Which Play the Role in Cellular Response against Oxidative/Nitrosative Stress: Current State, *Nutr. J.*, 2015, **15**(1), 71, DOI: 10.1186/s12937-016-0186-5.

36 A. Hanif, A. H. Ibrahim, S. Ismail, S. S. Al-Rawi, J. N. Ahmad, M. Hameed, G. Mustufa and S. Tanwir, Cytotoxicity against A549 Human Lung Cancer Cell Line via the Mitochondrial Membrane Potential and Nuclear Condensation Effects of Nepeta Paulsenii Briq., a Perennial Herb, *Molecules*, 2023, **28**(6), 2812, DOI: 10.3390/molecules28062812.

37 K. N. Patel, P. G. Trivedi, M. S. Thakar, K. V. Prajapati, D. K. Prajapati and G. M. Sindhav, Gold Nanoparticles Synthesis Using Gymnosporia Montana L. and Its Biological Profile: A Pioneer Report, *J. Genet. Eng. Biotechnol.*, 2023, **21**(1), 71, DOI: 10.1186/s43141-023-00525-6.

38 P. Conflitti, S. Raniolo and V. Limongelli, Perspectives on Ligand/Protein Binding Kinetics Simulations: Force Fields, Machine Learning, Sampling, and User-Friendliness, *J. Chem. Theory Comput.*, 2023, **19**(18), 6047–6061, DOI: 10.1021/acs.jctc.3c00641.

39 A. Stank, D. B. Kokh, J. C. Fuller and R. C. Wade, Protein Binding Pocket Dynamics, *Acc. Chem. Res.*, 2016, **49**(5), 809–815, DOI: 10.1021/acs.accounts.5b00516.

40 N. A. Gonzalez, B. A. Li and M. E. McCully, The Stability and Dynamics of Computationally Designed Proteins, *Protein Eng. Des. Sel.*, 2022, **35**, 1–10, DOI: 10.1093/protein/gzac001.

41 C. C. David and D. J. Jacobs, Principal Component Analysis: A Method for Determining the Essential Dynamics of, *Proteins*, 2014, 193–226, DOI: 10.1007/978-1-62703-658-0_11.

42 S. A. Hollingsworth and R. O. Dror, Molecular Dynamics Simulation for All, *Neuron*, 2018, **99**(6), 1129–1143, DOI: 10.1016/j.neuron.2018.08.011.

43 M. Karplus and J. A. McCammon, Molecular Dynamics Simulations of Biomolecules, *Nat. Struct. Biol.*, 2002, **9**(9), 646–652, DOI: 10.1038/nsb0902-646.

44 S. Genheden and U. Ryde, The MM/PBSA and MM/GBSA Methods to Estimate Ligand-Binding Affinities, *Expert Opin. Drug Discov.*, 2015, **10**(5), 449–461, DOI: 10.1517/17460441.2015.1032936.

45 M. De Vivo, M. Masetti, G. Bottegoni and A. Cavalli, Role of Molecular Dynamics and Related Methods in Drug Discovery, *J. Med. Chem.*, 2016, **59**(9), 4035–4061, DOI: 10.1021/acs.jmedchem.5b01684.

46 A. Daina, O. Michielin and V. Zoete, SwissADME: A Free Web Tool to Evaluate Pharmacokinetics, Drug-Likeness and Medicinal Chemistry Friendliness of Small Molecules, *Sci. Rep.*, 2017, 7(1), 42717, DOI: 10.1038/srep42717.